Subsurface stress evolution under orthotropic wear and frictional contact conditions

Javier M. Juliá, Luis Rodríguez-Tembleque [*]

Escuela Técnica Superior de Ingeniería, Universidad de Sevilla, Camino de los Descubrimientos s/n, Sevilla 41092, Spain

ARTICLE INFO

ABSTRACT

This work presents a computational framework to study the evolution of the subsurface stresses in 3D solids under orthotropic frictional contact and wear conditions. The formulation is based on the influence coefficients methodology to relate the discrete elastic response (i.e., displacements and stresses) to the sampled excitation (i.e., surface contact tractions). The proposed methodology is validated by solving several benchmark problems and is applied to analyze how the subsurface stress distribution (i.e. maximum value and its location) – and its evolution – caused by orthotropic wear conditions are clearly affected not only by the considered wear problems (i.e., sliding wear or fretting wear) but also by the friction coefficient values and the sliding direction angle — relative to the tribological axes. Several numerical examples are presented to show the importance of these last two aspects when orthotropic wear conditions are considered. In other case, we could over- or underestimate the maximum values of the subsurface stresses during the wear process.

1. Introduction

Wear represents one of the limited number of ways in which mechanical components lose their usefulness [1]. Consequently, the economic implication of wear estimation and subsurface stresses prediction during the wear processes have a tremendous value to the industry, since it allows engineers to predict the useful life of a mechanical element, to organize maintenance checking periods, and, consequently, to reduce costs of inoperability. The analytical and numerical tools to estimate wear, subsurface stresses, etc, allow engineers in that way, not only in these predictions, but also to optimize the design of those mechanical components (i.e., selecting proper materials, shapes and surface finishing according to the mechanical and durability conditions).

Computational tools to solve contact problems start with the theoretical solutions proposed, among others, by Hertz [2], Cattaneo [3] and Mindlin [4]. A synthesis of these analytical solutions and approaches can be found in monographs of Johnson [5] or Goryacheva [6]. Since the analytical solutions are achievable only for simple geometries, boundary conditions, and mostly for linear materials, numerical solution techniques started to be developed at the end of the 20th century. The numerical solution techniques employ variational inequalities [7–9] and, nowadays, they are generally divided into two groups. One is the group of the finite element methods (FEM) [7,9–11], which are widely used, especially in the contact problems with large deformations and/or nonlinear elastic materials. These methods typically focus

on overall behavior and require a fine discretization of the contacting bodies. The other group is the boundary element methods (BEM) [8, 12], that are well-suited and efficient to solve concentrated contact problem with homogeneous elastic materials. The boundary value problem is transformed to a boundary integral equation. The dimensionality of the problem decreases and, consequently, the computational time also decreases significantly, since the influence coefficients methodology [13–15] considers only the influence coefficients of the boundary degrees of freedom involved in the contact problem. Furthermore, it allows to obtain a very good accuracy, with a low number of elements, computing the surface and subsurface contact stresses [16–18].

Solutions for wear problems stem from the works by Holm [19] and Archard [20], as well as the works of Rabinowicz, which are collected in his monographic book [1]. In the last 30 years, many researchers have proposed different theoretical models to predict wear under several contact conditions. After the pioneers works of Galin et al. [21,22], Kovalenko et al. [23,24], Kragelsky [25] and Komogortsev [26], a number of wear contact problems have been studied using analytical techniques. The fundamental works of Hills et al. [27,28] and Goryacheva et al. [29] presented analytical solutions on fretting wear problems. The works of Olofsson et al. [30], Enblom and Berg [31], Telliskivi [32] proposed different solution schemes for rolling contact problems. In the applied oriented article [33], Hegadekatte et al. developed solutions strategies for pin-on-disk and twin-disk tribometers

---

under sliding wear conditions. More recently, during the last ten years, Argatov et al. have been presenting analytical solutions in the context of contact of deformed solids under wear conditions. Argatov [34] and Argatov and Tato [35] presented asymptotic solutions for (3D and 2D, respectively) sliding wear contact problems. In their very recent contribution [36,37], Argatov and Chai analyzed the steady-state regime and the wearing-in period in frictional contact problems, and in the work [38] discussed different approaches – analytical and semi-analytical – to model fretting wear.

Many computational frameworks and numerical studies on wear have been also developed in the last years using different numerical techniques [39]. In the group of the FEM, it should be mentioned the pioneering methodologies and solution schemes proposed by Johansson [40] and Strömberg et al. [41–44]. They made it possible to solve contact problems under different wear conditions (i.e., fretting wear or sliding wear). These schemes were extended by Ireman et al. [45,46] to study wear in thermoelastic contact problems. Another numerical schemes based on the FEM were presented to study fretting wear problems by: McColl et al. [47], Chai et al. [48], Mary and Fouvry [49] and Bae et al. [50], and, to study sliding wear problems, by Paczelt and Mróz [51]. The latest works in the finite element context are focusing on non-matching meshes schemes, i.e., the works of Farah et al. [52] and Doca and Andrade Pires [53]. In the BEM and/or the influence coefficient methods group, we should consider the contributions of Sfantos and Aliabadi [54–56] and Paczelt et al. [57] to solve sliding wear problems. Nowell [58], Gallego et al. [59], Kim et al. [60] and Rodríguez-Tembleque et al. [61,62] developed formulations to solve the contact problem under fretting wear conditions, and Rodríguez-Tembleque et al. [63,64] for wear computing under rolling-contact conditions. All these works have showed the suitability of the FEM or the BEM to simulate wear under more realistic contact conditions.

The interest of these formulations lies in the fact that, in addition to allowing us to – virtually – compute the surface contact tractions or the morphology adopted by the contact surfaces, they also allow us to determine the subsurface stress distributions that are generated during the contact process. For this reason, several recent works, i.e., Guler at al. [65], Jin et al. [18] or Meshcheryakova and Goryacheva [66], continue studying more efficient and accurate techniques to compute the subsurface stresses, as well as the distribution they adopt under frictional contact or rolling-contact conditions. In this context, this work presents an influence coefficient formulation and a robust solution scheme to study the subsurface stresses in orthotropic contact problems under sliding wear and fretting wear conditions. Moreover, this computational framework is considered to study how the orthotropic tribological conditions (i.e., the orthotropic friction and wear laws, the values of friction coefficients intensity, the sliding direction or the wear evolution) affect the value of the maximum subsurface stresses and their location. Thus, to the best authors knowledge, this paper presents for the first time the calculation of subsurface stress distributions as a function of the friction coefficient intensity and wear regime, under orthotropic contact conditions. This is a very interesting issue since, for instance, a recent study [67] has revealed the relation between the subsurface stresses and the useful wear life in sliding contacts.

Finally, this paper is organized as follows: Section 2 presents the basic governing equations of this 3D orthotropic frictional contact problem description and the expressions to compute the subsurface stresses. The discrete formulation the problem and the non-linear solution scheme are presented in Section 3. Then, the methodology is applied in Section 4 to solve several contact problems under different orthotropic friction and wear conditions. These examples allow us to study how the subsurface stress distributions, the subsurface maximum values and their locations are affected by the orthotropic friction and wear laws, the friction coefficient intensities, the wear regimes (i.e., gross slip or partial slip) and the sliding direction. Finally, some concluding remarks are presented in Section 5.
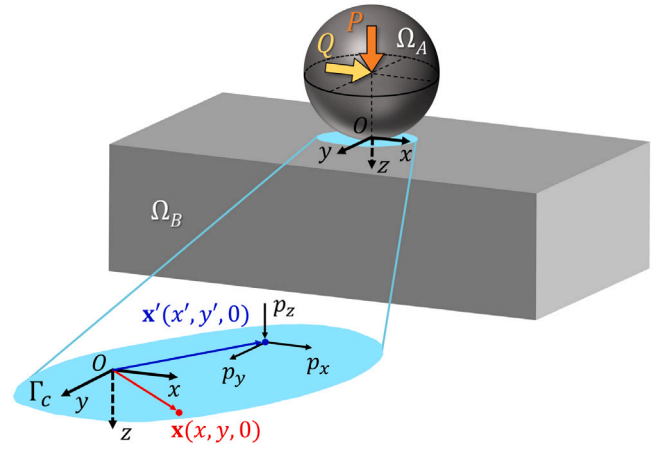

Fig. 1. Two elastic bodies (i.e., a sphere Ω_A over an elastic halfspace Ω_B) come into contact under the normal load P and the tangential load Q, being Γ_c the resulting contact area.

2. Governing equations for 3D orthotropic frictional contact problems

This section presents in detail the equations set that defines the 3D frictional contact problem of two solids, under wear conditions. The tribological – friction and wear – laws will be assumed to be orthotropic, considering an associated sliding rule. Firstly, we will start defining the contact kinematic variables, i.e., the normal gap and the tangential slip velocity, as a function of the solids displacements. Secondly, a half-space approximation will be considered to describe the relations between the contact tractions and the solids displacements. Thirdly, the frictional contact inequality constraints and the wear law will be presented, so that the restrictions for the contact kinematical variables and the contact tractions will be defined. Finally, the expressions to compute the subsurface stresses will presented as a function of the surface contact tractions.

2.1. Contact kinematics

The kinematic description of two elastic bodies (Ω^α, $\alpha = A, B$) in contact starts with the definition of a coordinate system $Oxyz$, which allows us to identify the position $\mathbf{x}$ of each particle of these two bodies. In that system, z points are normally oriented to the upper body and $\{x, y\}$ are tangentially directed (see Fig. 1). When the bodies come into contact at a certain pseudo-time instance τ, the deformation at the contact zone position $\mathbf{x}$ can be defined by the displacement difference: $\mathbf{u}(\mathbf{x}, \tau) = \mathbf{u}^{(A)}(\mathbf{x}, \tau) - \mathbf{u}^{(B)}(\mathbf{x}, \tau)$.

The separation between the two solids surfaces can be quantified by the normal contact gap

$$g_n(\mathbf{x}, \tau) = g_{n,o}(\tau) + \omega(\mathbf{x}, \tau) + u_n(\mathbf{x}, \tau) \tag{1}$$

and the tangential contact gap

$$\mathbf{g}_t(\mathbf{x}, \tau) = \mathbf{g}_{t,o}(\tau) + \mathbf{u}_t(\mathbf{x}, \tau). \tag{2}$$

In Eq. (1), $g_{n,o}(\tau) = g_g - g_o(\tau)$ (where g_g is the geometric gap and $g_o(\tau)$ is the rigid body rapprochement), $\omega(\mathbf{x}, \tau)$ is the wear gap (i.e., *wear depth*) and u_n is the relative normal displacement: $u_n(\mathbf{x}, \tau) = u_z^{(A)}(\mathbf{x}, \tau) - u_z^{(B)}(\mathbf{x}, \tau)$ whereas, in the Eq. (2), $\mathbf{g}_{t,o}(\tau)$ is the relative rigid tangential slip and $\mathbf{u}_t(\mathbf{x}, \tau) = [u_x(\mathbf{x}, \tau)\ u_y(\mathbf{x}, \tau)]^T$ is the relative tangential displacement: $\mathbf{u}_t(\mathbf{x}, \tau) = \mathbf{u}_t^{(A)}(\mathbf{x}, \tau) - \mathbf{u}_t^{(B)}(\mathbf{x}, \tau)$.

2.2. Half-space approximation

The displacement difference $\mathbf{u}(\mathbf{x}, \tau)$ can be obtained by half-space approach proposed by Kalker [13], which assumes that the contacting bodies are constituted by homogeneous linear elastic materials, the contact area is very small compared with the contacting bodies (and consequently, it is flat), the geometries are sufficiently smooth and, finally, the inertia effects are ignored, so a quasi-static description is considered.

Under the previous assumptions, the classical Boussinesq and Cerruti solutions can be adopted, therefore, according to Johnson [5] or Kalker [13], at a certain pseudo-time instance τ, the relation between the deformation $\mathbf{u}$ at point $\mathbf{x}$ and the contact traction $\mathbf{p}$ on points $\mathbf{x}' \in \Gamma_c$ (see Fig. 1) is given by:

$$\mathbf{u}(\mathbf{x}, \tau) = \int \int_{\Gamma_c(\tau)} \mathbf{A}(\mathbf{x}, \mathbf{x}') \, \mathbf{p}(\mathbf{x}', \tau) \, dx' dy' \tag{3}$$

In the expression above, the kernel function $\mathbf{A}(\mathbf{x}, \mathbf{x}')$ gives the influence of a unit traction at $\mathbf{x}'$ on a deformation at $\mathbf{x}$ and can be written as

$$\mathbf{A}(\mathbf{x}, \mathbf{x}') = \begin{bmatrix} A_{xx}(\mathbf{x}, \mathbf{x}') & A_{xy}(\mathbf{x}, \mathbf{x}') & A_{xz}(\mathbf{x}, \mathbf{x}') \\ A_{yx}(\mathbf{x}, \mathbf{x}') & A_{yy}(\mathbf{x}, \mathbf{x}') & A_{yz}(\mathbf{x}, \mathbf{x}') \\ A_{zx}(\mathbf{x}, \mathbf{x}') & A_{zy}(\mathbf{x}, \mathbf{x}') & A_{zz}(\mathbf{x}, \mathbf{x}') \end{bmatrix} \tag{4}$$

where

$$
\begin{aligned}
A_{xx}(\mathbf{x}, \mathbf{x}') &= \frac{1}{\pi G}\left(\frac{1-\nu}{s} + \frac{(x'-x)^2}{s^3}\right), \\
A_{yy}(\mathbf{x}, \mathbf{x}') &= \frac{1}{\pi G}\left(\frac{1-\nu}{s} + \frac{(y'-y)^2}{s^3}\right), \\
A_{zz}(\mathbf{x}, \mathbf{x}') &= \frac{1}{\pi G}\left(\frac{1-\nu}{s}\right), \\
A_{xy}(\mathbf{x}, \mathbf{x}') &= \frac{\nu}{\pi G}\left(\frac{(x'-x)(y'-y)}{s^3}\right), \quad A_{yx}(\mathbf{x}, \mathbf{x}') = A_{xy}(\mathbf{x}, \mathbf{x}'), \\
A_{xz}(\mathbf{x}, \mathbf{x}') &= \frac{K}{\pi G}\left(\frac{x'-x}{s^2}\right), \qquad\qquad A_{zx}(\mathbf{x}, \mathbf{x}') = -A_{xz}(\mathbf{x}, \mathbf{x}'), \\
A_{yz}(\mathbf{x}, \mathbf{x}') &= \frac{K}{\pi G}\left(\frac{y'-y}{s^2}\right), \qquad\qquad A_{zy}(\mathbf{x}, \mathbf{x}') = -A_{yz}(\mathbf{x}, \mathbf{x}'),
\end{aligned}
\tag{5}
$$

being $s = \sqrt{(x'-x)^2 + (y'-y)^2}$ and G, ν and K are the material parameters defined as

$$
\begin{aligned}
\frac{1}{G} &= \frac{1}{2}\left(\frac{1}{G^{(A)}} + \frac{1}{G^{(B)}}\right), \\
\frac{\nu}{G} &= \frac{1}{2}\left(\frac{\nu^{(A)}}{G^{(A)}} + \frac{\nu^{(B)}}{G^{(B)}}\right), \\
K &= \frac{G}{4}\left(\frac{1-2\nu^{(A)}}{G^{(A)}} - \frac{1-2\nu^{(B)}}{G^{(B)}}\right).
\end{aligned}
\tag{6}
$$

The expressions in Eq. (5) allows the kernel function to be also written as: $\mathbf{A}(\mathbf{x}, \mathbf{x}') = \mathbf{A}(\mathbf{x}' - \mathbf{x})$, which indicates that the influence coefficients depend on the relative positions of the two surface points $\mathbf{x}$ and $\mathbf{x}'$.

2.3. Contact restrictions

The Signorini's conditions for unilateral contact can be expressed in the form of complementary relations, for the normal gap $g_n(\mathbf{x}, \tau)$ and the normal contact pressure $p_n = p_z(\mathbf{x}, \tau)$, as

$$g_n \geq 0, \quad p_n \geq 0, \quad g_n p_n = 0, \tag{7}$$

for every point in the contact zone (i.e., $\mathbf{x} \in \Gamma_c$).

Similarly, the fulfillment of an orthotropic friction law is guaranteed by the complementary relations

$$f(p_n, \mathbf{p}_t) \leq 0, \quad \lambda \geq 0, \quad \lambda \, f(p_n, \mathbf{p}_t) = 0, \tag{8}$$

where, according to [68–71], $\lambda = \|\dot{\mathbf{g}}_t\|_\mu^*$, $\mathbf{p}_t$ is the tangential contact traction vector ($\mathbf{p}_t = [p_x(\mathbf{x}, \tau) \; p_y(\mathbf{x}, \tau)]^T$) and $f(\mathbf{p}_t, p_n) = \|\mathbf{p}_t\|_\mu - p_n$

is a function which allows us to define the orthotropic friction limit: $f(\mathbf{p}_t, p_n) = 0$ (see Fig. 2(a)).

In the previous paragraph, the elliptic norm $\| \bullet \|_\mu$ is defined so that

$$\|\mathbf{p}_t\|_\mu = \sqrt{\left(p_{e_1}/\mu_1\right)^2 + \left(p_{e_2}/\mu_2\right)^2}, \tag{9}$$

being μ_1 and μ_2 the principal friction coefficients in the directions $\{e_1, e_2\}$. Moreover, the norm $\| \bullet \|_\mu^*$ is dual of $\| \bullet \|_\mu$ and consequently,

$$\|\dot{\mathbf{g}}_t\|_\mu^* = \sqrt{(\mu_1 \dot{g}_{e_1})^2 + (\mu_2 \dot{g}_{e_2})^2}. \tag{10}$$

It is important to mention that, in Eq. (9) and in Eq. (10), the tangential contact tractions components and the tangential slip velocity components are defined in the tribological axes $\{e_1, e_2\}$ as:

$$\begin{bmatrix} p_{e_1} \\ p_{e_2} \end{bmatrix} = \begin{bmatrix} \cos\beta & \sin\beta \\ -\sin\beta & \cos\beta \end{bmatrix} \begin{bmatrix} p_x \\ p_y \end{bmatrix} \tag{11}$$

and

$$\begin{bmatrix} \dot{g}_{e_1} \\ \dot{g}_{e_2} \end{bmatrix} = \begin{bmatrix} \cos\beta & \sin\beta \\ -\sin\beta & \cos\beta \end{bmatrix} \begin{bmatrix} \dot{g}_x \\ \dot{g}_y \end{bmatrix}, \tag{12}$$

where the angle β is defined in Fig. 2(b) as the tribological axes angle orientation. In the expression above, the tangential slip velocity $\dot{\mathbf{g}}_t$ can be expressed at time τ_k as follows: $\dot{\mathbf{g}}_t \approx \Delta \mathbf{g}_t / \Delta\tau$ (see Rodríguez-Tembleque et al. [68]), where $\Delta \mathbf{g}_t = \mathbf{g}_t(\tau_k) - \mathbf{g}_t(\tau_{k-1})$ and $\Delta\tau = \tau_k - \tau_{k-1}$.

In this way, the possible states for each contact point on Γ_c are characterized by

$$
\begin{array}{llll}
\text{No contact:} & p_n = 0, & g_n \geq 0, & \mathbf{p}_t = \mathbf{0}, \\
\text{Contact-Stick:} & p_n \geq 0, & g_n = 0, & \dot{\mathbf{g}}_t = \mathbf{0}, \\
\text{Contact-Slip:} & p_n \geq 0, & g_n = 0, & \mathbf{p}_t = -p_n \, \mathbb{M}^2 \dot{\mathbf{g}}_t / \|\dot{\mathbf{g}}_t\|_\mu^*,
\end{array}
\tag{13}
$$

being

$$\mathbb{M} = \begin{bmatrix} \mu_1 & 0 \\ 0 & \mu_2 \end{bmatrix}. \tag{14}$$

The normal contact constraints presented in Eq. (7) can be formulated in a more compact form using augmented variables and projection functions, as:

$$p_n - \mathbb{P}_{\mathbb{R}^+}(p_n^*) = 0, \tag{15}$$

where $\mathbb{P}_{\mathbb{R}^+}(\bullet)$ is the normal projection function ($\mathbb{P}_{\mathbb{R}^+}(\bullet) = max(0, \bullet)$) and $p_n^* = p_n + r_n g_n$ is the augmented normal traction. The parameter r_n is the normal dimensional penalization parameter ($r_n \in \mathbb{R}^+$). Moreover, the frictional contact constraints presented in Eq. (8) can also be formulated using augmented variables and projection functions, as:

$$\mathbf{p}_t - \mathbb{P}_{\mathbb{E}_\rho}(\mathbf{p}_t^*) = 0, \tag{16}$$

where $\mathbf{p}_t^* = \mathbf{p}_t - r_t \mathbb{M}^2 \dot{\mathbf{g}}_t$ ($r_t \in \mathbb{R}^+$) is the augmented tangential traction and $\mathbb{P}_{\mathbb{E}_\rho}(\bullet) : \mathbb{R}^2 \longrightarrow \mathbb{R}^2$ is the tangential projection function defined in [68] as

$$\mathbb{P}_{\mathbb{E}_\rho}(\mathbf{p}_t^*) = \begin{cases} \mathbf{p}_t^* & \text{if} \quad \|\mathbf{p}_t^*\|_\mu < \rho, \\ \rho \, \mathbf{p}_t^* / \|\mathbf{p}_t^*\|_\mu & \text{if} \quad \|\mathbf{p}_t^*\|_\mu \geq \rho, \end{cases} \tag{17}$$

with $\rho = |\mathbb{P}_{\mathbb{R}^+}(p_n^*)|$. Therefore, Eqs. (15) and (16) constitute the orthotropic frictional contact restrictions for every point: $\mathbf{x} \in \Gamma_c$.

2.4. Wear law

Wear process evolves over time, so the Holm–Archard's wear law [1] might be expressed locally for an infinitesimally small apparent contact area and in a differential form to compute the wear depth: $\omega(\mathbf{x}, \tau)$. Therefore, a quasi-steady-state wear approximation, similarly to the computational works [61,63,64,72–77], is considered in the following wear rate form:

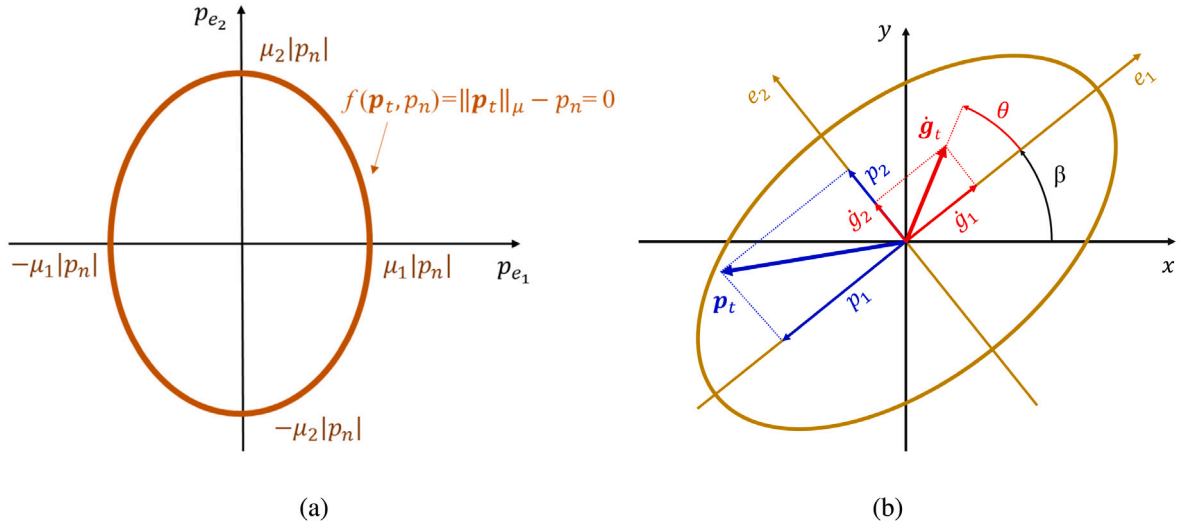$$\dot{\omega} = i_w \, |p_n| \, \|\dot{\mathbf{g}}_t\|, \tag{18}$$

Fig. 2. (a) Orthotropic sliding surface in tribological coordinate axes e_1 and e_2. (b) Associated sliding rule in coordinate axes e_1 and e_2. The axes e_1 and e_2 form an angle β (counter-clock-wise) with the halfspace coordinate axes x and y, respectively. .

where i_w is the dimensional wear coefficient.

Due to orthotropic tribological properties are considered in this work, an orthotropic wear law [64,70,71] is assumed. Consequently, i_w should be function of the sliding direction parameter θ [64] (see Fig. 2(b)), i.e., the angle between the given direction ($\mathbf{e}_1$) and the sliding direction ($\dot{\mathbf{g}}_t/\|\dot{\mathbf{g}}_t\|$), as:

$$i_w(\theta) = \sqrt{(i_1 \cos \theta)^2 + (i_2 \sin \theta)^2}. \tag{19}$$

In the expression above, $\cos \theta = \dot{g}_{e_1}/\|\dot{\mathbf{g}}_t\|$, $\sin \theta = \dot{g}_{e_2}/\|\dot{\mathbf{g}}_t\|$, and i_1 and i_2 are the principal intensity wear coefficients.

In this work, it is postulated that the wear rate is proportional to the friction dissipation energy, friction and wear coefficients are related through the constant c as: $i_1 = c \, \mu_1$ and $i_2 = c \, \mu_2$.

According to [64], wear coefficient can be written as

$$i_w = \|\dot{\mathbf{g}}_t\|_i/\|\dot{\mathbf{g}}_t\|, \tag{20}$$

where

$$\|\dot{\mathbf{g}}_t\|_i = \sqrt{(i_1 \dot{g}_{e_1})^2 + (i_2 \dot{g}_{e_2})^2}. \tag{21}$$

Consequently, the orthotropic wear law Eq. (18) can be rewritten as

$$\dot{\omega} = |p_n| \, \|\dot{\mathbf{g}}_t\|_i. \tag{22}$$

For quasi-static contact problems derivatives can be expressed in an incremental form: $\dot{\omega} \simeq \Delta\omega = \omega(\tau_k) - \omega(\tau_{k-1})$ and $\dot{\mathbf{g}} \simeq \Delta\mathbf{g} = \mathbf{g}(\tau_k) - \mathbf{g}(\tau_{k-1})$, therefore wear depth at the instant τ_k can be computed as

$$\omega(\tau_k) = \omega(\tau_{k-1}) + p_n(\tau_k) \, \| \mathbf{g}_t(\tau_k) - \mathbf{g}_t(\tau_{k-1})\|_i. \tag{23}$$

2.5. Subsurface stresses

Finally, the subsurface elastic stresses at point $\mathbf{x} \in \Omega^{(\alpha)}$ ($\alpha = A, B$) due to known surface tractions on a point $\mathbf{x}' \in \Gamma_c$ (see Fig. 3) can be presented in a very compact form as

$$\sigma(\mathbf{x}, \tau) = \int\!\!\int_{\Gamma_c(\tau)} \mathbf{T}(\mathbf{x}, \mathbf{x}') \, \mathbf{p}(\mathbf{x}', \tau) \, dx' dy, \tag{24}$$

where, similarly to the kernel function $\mathbf{A}(\mathbf{x}, \mathbf{x}')$, the influence coefficients of the kernel function $\mathbf{T}(\mathbf{x}, \mathbf{x}')$ depend on the relative positions of the two surface points $\mathbf{x}$ and $\mathbf{x}'$, therefore $\mathbf{T}(\mathbf{x}, \mathbf{x}') = \mathbf{T}(\mathbf{x}' - \mathbf{x})$.

For the sake of clarity, the expression above is rewritten as

$$\sigma_{ij}(\mathbf{x}, \tau) = \int\!\!\int_{\Gamma_c(\tau)} T_{ij}^{Sx}(\mathbf{x}' - \mathbf{x}) \, p_x(\mathbf{x}', \tau) + T_{ij}^{Sy}(\mathbf{x}' - \mathbf{x}) \, p_y(\mathbf{x}', \tau)$$
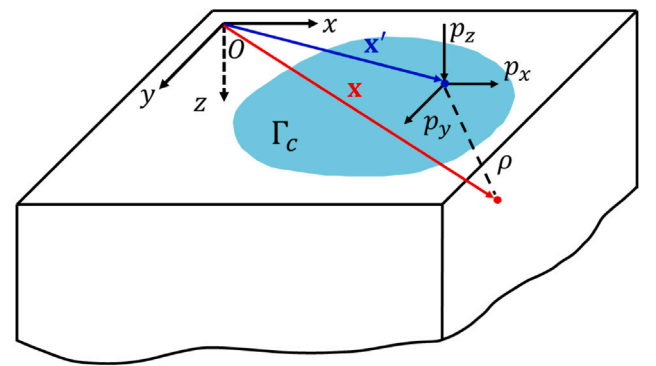

Fig. 3. Half-space approximation scheme where subsurface elastic stresses at point $\mathbf{x} \in \Omega^{(\alpha)}$ ($\alpha = A, B$) caused by known surface tractions on a point $\mathbf{x}' \in \Gamma_c$.

$$+ \; T_{ij}^N(\mathbf{x}' - \mathbf{x}) \, p_n(\mathbf{x}', \tau) \, dx' dy' \tag{25}$$

where $T_{ij}^N(x, y, z)$, $T_{ij}^{Sx}(x, y, z)$ and $T_{ij}^{Sy}(x, y, z)$ are the stress solutions due to a unit normal force, a unit shear force along the x axis and a unit shear force along the y axis, respectively, at the surface origin of a half space. The expressions of these functions can be found in Appendix A.

3. Discrete formulation

This section presents the discrete formulation of the equation set defined in Section 2. First, we start presenting the discrete influence coefficient equations between the discrete contact tractions and solids displacements. Next, the discrete expressions for the contact kinematic variables and the subsurface stresses equations will be described in detail. Finally, to conclude this section, we will describe the solution scheme proposed to compute the discrete contact tractions, kinematic variable and subsurface stresses, subjected to the discrete contact restrictions.

3.1. Discrete contact problem approximation

The discretization of the problem focuses on a rectangular potential contact area, which contains the true contact area. A rectangular mesh is placed on this 2D region, with $N_e = N_x \times N_y$ elements of size $\Delta_x \times \Delta_y$ (see Fig. 4). The coordinates of the center of the element I are denoted by $\mathbf{x}_I = [x_I, y_I, 0]^T$.
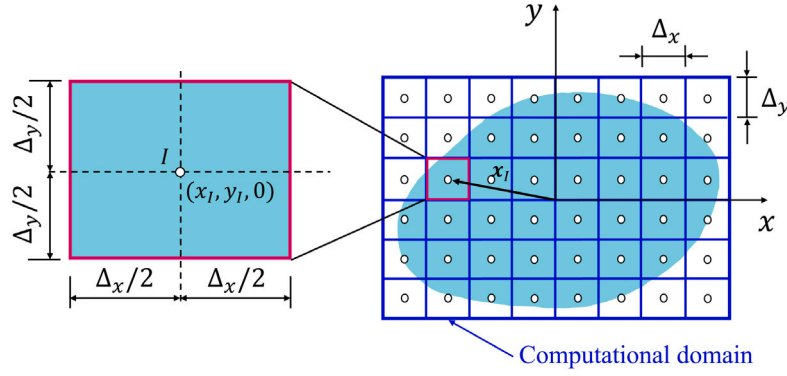
Fig. 4. The potential contact zone is meshed with $N_e = N_x \times N_y$ elements of size $\Delta_x \times \Delta_y$.

In this numerical modeling, tractions $\mathbf{p}$ in the surface integral Eq. (3) are approximated by element-wise constant functions. This cell-centered discretization of the integral Eq. (3) allows us to rewrite this expression, for each contacting element I, as the summation of the products of influence coefficients A_{IJ}^{ij} (i, j corresponding to x, y and z) and nodal pressures p_{Jj} at element J:

$$u_{Ix}^{(k)} = \sum_{J=1}^{N_e} A_{IJ}^{xx} p_{Jx}^{(k)} + A_{IJ}^{xy} p_{Jy}^{(k)} + A_{IJ}^{xz} p_{Jz}^{(k)},$$

$$u_{Iy}^{(k)} = \sum_{J=1}^{N_e} A_{IJ}^{yx} p_{Jx}^{(k)} + A_{IJ}^{yy} p_{Jy}^{(k)} + A_{IJ}^{yz} p_{Jz}^{(k)}, \qquad (26)$$

$$u_{Iz}^{(k)} = \sum_{J=1}^{N_e} A_{IJ}^{zx} p_{Jx}^{(k)} + A_{IJ}^{zy} p_{Jy}^{(k)} + A_{IJ}^{zz} p_{Jz}^{(k)}.$$

where, $u_{Ii}^{(k)}$ the deformation in i-direction of element I at instant τ_k. Influence coefficient A_{IJ}^{ij} represents the influence to the i-direction deformation on element I, caused by a unit j-direction traction on another element J. It is computed by integrating Eq. (3) over a single element J, with respect to an observation point at the center of element I (see [13–15]). The explicit expressions of the influence coefficients A_{IJ}^{ij} are presented in Appendix B.

Assembling the coefficients A_{IJ}^{ij} in the matrix $\mathbf{A}_{ij}$: $\left(\mathbf{A}_{ij} \right)_{IJ} = A_{IJ}^{ij}$, the Eq. (26) can be expressed as $\mathbf{u}^{(k)} = \mathbf{A}\,\mathbf{p}^{(k)}$, i.e.,

$$\begin{bmatrix} \mathbf{u}_x \\ \mathbf{u}_y \\ \mathbf{u}_z \end{bmatrix}^{(k)} = \begin{bmatrix} \mathbf{A}_{xx} & \mathbf{A}_{xy} & \mathbf{A}_{xz} \\ \mathbf{A}_{yx} & \mathbf{A}_{yy} & \mathbf{A}_{yz} \\ \mathbf{A}_{zx} & \mathbf{A}_{zy} & \mathbf{A}_{zz} \end{bmatrix} \begin{bmatrix} \mathbf{p}_x \\ \mathbf{p}_y \\ \mathbf{p}_z \end{bmatrix}^{(k)}, \qquad (27)$$

where vector $\mathbf{u}^{(k)}$ and vector $\mathbf{p}^{(k)}$ contain the deformation components and the contact tractions of each element I at instant τ_k, respectively. For the sake of clarity, Eq. (28) is rearranged as

$$\begin{bmatrix} \mathbf{u}_n \\ \mathbf{u}_t \end{bmatrix}^{(k)} = \begin{bmatrix} \mathbf{A}_{nn} & \mathbf{A}_{nt} \\ \mathbf{A}_{tn} & \mathbf{A}_{tt} \end{bmatrix} \begin{bmatrix} \mathbf{p}_n \\ \mathbf{p}_t \end{bmatrix}^{(k)}, \qquad (28)$$

where $\mathbf{u}_n^{(k)} = \mathbf{u}_z^{(k)}$, $\mathbf{p}_n^{(k)} = \mathbf{p}_z^{(k)}$, $\mathbf{u}_t^{(k)}$ contains the tangential deformation components of each element I (i.e., $(\mathbf{u}_t^{(k)})_I = [\,(\mathbf{u}_x^{(k)})_I \quad (\mathbf{u}_y^{(k)})_I\,]^T$) and $\mathbf{p}_t^{(k)}$ the contact traction components of each element I (i.e., $(\mathbf{p}_t^{(k)})_I = [\,(\mathbf{p}_x^{(k)})_I \quad (\mathbf{p}_y^{(k)})_I\,]^T$).

3.2. Discrete contact kinematic variables

The normal gap (1) and the tangential contact slip (2) of each element I, at instant τ_k, can be stored as

$$\mathbf{g}_n^{(k)} = \mathbf{g}_{n,o}^{(k)} + \mathbf{w}^{(k)} + \mathbf{u}_n^{(k)} \qquad (29)$$

and

$$\mathbf{g}_t^{(k)} = \mathbf{g}_{t,o}^{(k)} + \mathbf{u}_t^{(k)} \qquad (30)$$

respectively. In Eq. (29), $\mathbf{g}_{z,o}^{(k)}$ is the bodies' rapprochement vector, whereas, in Eq. (30), $\mathbf{g}_{x,o}^{(k)}$ and $\mathbf{g}_{y,o}^{(k)}$ are vectors which contains the relative rigid tangential slip displacement components of each element I. In the expressions above, $\mathbf{u}_n^{(k)}$ and $\mathbf{u}_t^{(k)}$ are obtained from Eq. (28), where $\mathbf{p}_n^{(k)}$ and $\mathbf{p}_t^{(k)}$ satisfy, respectively, the normal and tangential contact restrictions presented in Eq. (15) and (16).

Finally, vector $\mathbf{w}^{(k)}$ contains the wear depth on each element I computed according to Eq. (31), i.e.,

$$(\mathbf{w}^{(k)})_I = (\mathbf{w}^{(k-1)})_I + (\mathbf{p}_n^{(k)})_I \,||(\mathbf{g}_t^{(k)})_I - (\mathbf{g}_t^{(k-1)})_I||_i. \qquad (31)$$

3.3. Discrete subsurface stresses equations

The subsurface stresses can be computed from discrete expression of Eq. (25) for a set of interior points (i.e., $\mathbf{x}_I \in \Omega^{(\alpha)}$ ($\alpha = A, B$) being $I = 1...N_i$), as,

$$(\sigma_{ij}^{(k)})_I = \sum_{J=1}^{N_e} (B_{ij}^{Sx})_{IJ} p_{Jx}^{(k)} + (B_{ij}^{Sy})_{IJ} p_{Jy}^{(k)} + (B_{ij}^{N})_{IJ} p_{Jz}^{(k)} \qquad (32)$$

where $(\sigma_{ij}^{(k)})_I$ is the value for the stress at point $\mathbf{x}_I$ on instant τ_k: $\sigma_{ij}(\mathbf{x}_I, \tau_k)$, due to the known surface contact tractions $\mathbf{p}^{(k)}$. Moreover, the influence coefficients $(B_{ij}^{Sx})_{IJ}$, $(B_{ij}^{Sy})_{IJ}$ and $(B_{ij}^{N})_{IJ}$ are computed as

$$(B_{ij}^{Sx})_{IJ} = \int_{x_-}^{x_+} \int_{y_-}^{y_+} T_{ij}^{Sx}(x, y, z_I)\, dx' dy',$$

$$(B_{ij}^{Sy})_{IJ} = \int_{x_-}^{x_+} \int_{y_-}^{y_+} T_{ij}^{Sy}(x, y, z_I)\, dx' dy', \qquad (33)$$

$$(B_{ij}^{N})_{IJ} = \int_{x_-}^{x_+} \int_{y_-}^{y_+} T_{ij}^{N}(x, y, z_I)\, dx' dy'.$$

The influence coefficient $(B_{ij}^{N})_{IJ}$ represents the influence to the σ_{ij}-stress on $\mathbf{x}_I$, caused by a unit normal traction applied on element J. Similarly, coefficients $(B_{ij}^{Sx})_{IJ}$ (or $(B_{ij}^{Sy})_{IJ}$) represents the influence to the σ_{ij}-stress caused by a unit tangential traction on x-direction (or on y-direction), applied on element J. The subsurface influence coefficients (33) are calculated according to [78] and detailed in Appendix C.

Finally, Eq. (32) can be presented in the following matrix form

$$\boldsymbol{\sigma}_{ij}^{(k)} = \mathbf{B}_{ij}^{Sx} \mathbf{p}_x^{(k)} + \mathbf{B}_{ij}^{Sy} \mathbf{p}_y^{(k)} + \mathbf{B}_{ij}^{N} \mathbf{p}_z^{(k)} \qquad (34)$$

where $\boldsymbol{\sigma}_{ij}^{(k)}$ is a N_i-dimensional vector containing the value of the stress component σ_{ij} on every subsurface point $\mathbf{x}_I \in \Omega^{(\alpha)}$ at instant τ_k.

3.4. Solution scheme

The discrete equations set (26)–(33) allows us to compute the subsurface stresses evolution caused by orthotropic wear and contact conditions. That set of equations can be solved using an iterative Uzawa scheme similar to [61,63,64,79–82]. To compute the variables at the instant or load step (k),

(I) Initialize $\mathbf{p}_n^{(0)} = \mathbf{p}_n^{(k-1)}$, $\mathbf{p}_t^{(0)} = \mathbf{p}_t^{(k-1)}$ and $\mathbf{w}^{(0)} = \mathbf{w}^{(k-1)}$ and iterate using ($n = 0, 1, 2, 3, \ldots$) index.

(II) Compute:

$$
\begin{bmatrix} \mathbf{g}_n \\ \mathbf{g}_t \end{bmatrix}^{(n)} = \begin{bmatrix} \mathbf{g}_{n,o} \\ \mathbf{g}_{t,o} \end{bmatrix}^{(k)} + \begin{bmatrix} \mathbf{w} \\ \mathbf{0} \end{bmatrix}^{(n)} + \begin{bmatrix} \mathbf{A}_{nn} & \mathbf{A}_{nt} \\ \mathbf{A}_{tn} & \mathbf{A}_{tt} \end{bmatrix} \begin{bmatrix} \mathbf{p}_n \\ \mathbf{p}_t \end{bmatrix}^{(n)},
$$

(35)

(III) Update contact tractions on every element I:

$$(\mathbf{p}_n^{(n+1)})_I = \mathbb{P}_{\mathbb{R}^+}(\, (\mathbf{p}_n^{(n)})_I + r_n(\mathbf{g}_n^{(n+1)})_I \,)$$

$$(\mathbf{p}_t^{(n+1)})_I = \mathbb{P}_{\mathbb{E}_\rho}(\, (\mathbf{p}_t^{(n)})_I - r_t \, \mathbb{M}^2 (\Delta\mathbf{g}_t^{(n+1)})_I \,),$$

where $(\Delta\mathbf{g}_t^{(n+1)})_I = (\mathbf{g}_t^{(n+1)})_I - (\mathbf{g}_t^{(0)})_I$ and $\rho = (\mathbf{p}_n^{(n+1)})_I$.

(IV) Update accumulated wear depth:

$$(\mathbf{w}^{(n+1)})_I = (\mathbf{w}^{(0)})_I + |(\, \mathbf{p}_n^{(n+1)})_I| \, \|(\Delta\mathbf{g}_t^{(n+1)})_I\|_i.$$

(V) Compute the error:

$$\Psi(\mathbf{p}_c^{(n+1)}) = \|\mathbf{p}_n^{(n+1)} - \mathbf{p}_n^{(n)}\| + \|\mathbf{p}_t^{(n+1)} - \mathbf{p}_t^{(n)}\|.$$

   (a) If $\Psi(\mathbf{p}_c^{(n+1)}) \leq \varepsilon$, the solution for the instant (k) is reached. If the applied boundary condition are the external normal load ($P^{(k)}$) and/or the tangential load ($Q^{(k)}$), the resultant contact loads on the contact zone (Γ_c) have to be also computed before reaching the solution for instant (k):

$$P^{(n+1)} = \Delta_x \, \Delta_y \, \sum_{I=1}^{N_e}(\mathbf{p}_n^{(n+1)})_I, \tag{36}$$

$$\mathbf{Q}^{(n+1)} = \Delta_x \, \Delta_y \, \sum_{I=1}^{N_e}(\mathbf{p}_t^{(n+1)})_I, \tag{37}$$

therefore,

     (a.1) If $P^{(n+1)} > P^{(k)} + \varepsilon_{load}$ or $P^{(n+1)} < P^{(k)} - \varepsilon_{load}$, modify $\mathbf{g}_{o,n}^{(k)} \to \mathbf{g}_{o,n}^{(k)} \mp \Delta\mathbf{g}_{o,n}^{(n)}$. Moreover, if $\|\mathbf{Q}^{(n+1)}\| > Q^{(k)} + \varepsilon_{load}$ or $\|\mathbf{Q}^{(n+1)}\| < Q^{(k)} - \varepsilon_{load}$, modify $\mathbf{g}_{o,t}^{(k)} \to \mathbf{g}_{o,t}^{(k)} \mp \Delta\mathbf{g}_{o,t}^{(n)}$, and return to (II).

     (a.2) Otherwise, the solution for instant (k) is reached, so $\mathbf{p}_n^{(k)} = \mathbf{p}_n^{(n+1)}$, $\mathbf{p}_t^{(k)} = \mathbf{p}_t^{(n+1)}$, $\mathbf{g}_n^{(k)} = \mathbf{g}_n^{(n+1)}$, $\mathbf{g}_t^{(k)} = \mathbf{g}_t^{(n+1)}$ and $\mathbf{w}^{(k)} = \mathbf{w}^{(n+1)}$.

   (b) Otherwise, return to (II) evaluating: $\mathbf{p}_n^{(n)} = \mathbf{p}_n^{(n+1)}$, $\mathbf{p}_t^{(n)} = \mathbf{p}_t^{(n+1)}$ and $\mathbf{w}^{(n)} = \mathbf{w}^{(n+1)}$, and iterate until the convergence is reached.

(VI) Finally, compute the subsurface stresses for the load step (k), i.e., $\sigma_{ij}^{(k)}$, according to the Eq. (34).

Once the solution at instant (k) is reached, the solution for the next instant is achieved by returning to (I).

4. Numerical results

This section presents several numerical examples which allow us to validate the proposed formulation and to study how the subsurface stresses maximum values and their locations are affected by the orthotropic friction and wear laws, the friction coefficient intensities, the wear regimes (i.e., gross slip or partial slip) and the sliding direction. For this purpose, the section have been divided into two blocks. Firstly, in Section 4.1, we study the subsurface stress evolution under sliding-wear conditions and, secondly, in Section 4.2, we study the subsurface stress evolution due to fretting wear conditions.

In Section 4.1, we will first validate the proposed numerical scheme by solving the spherical pin sliding on a disk under isotropic friction and wear conditions. Results will be compared with analytical solutions. Then, we will move on to study the influence of the friction intensity on the subsurface stress evolution caused by isotropic sliding wear conditions. To conclude this section, the subsurface stress evolution caused by orthotropic sliding wear conditions will be analyzed. In this case, due to its influence on the friction intensity and wear effective coefficient value, the sliding direction will be studied.

Section 4.2 will present the subsurface stresses evolution with the number of cycles (N), under orthotropic fretting wear conditions. As we have mentioned, friction intensity and wear effective coefficient value are affected by the sliding direction. Consequently, the fretting wear regimes (i.e., gross slip or partial slip) is controlled by the sliding direction and, therefore, we will see how the subsurface stress evolution is clearly affected by the sliding direction.

4.1. Subsurface stress evolution under sliding-wear conditions

Let us consider a spherical pin sliding on a disk, as shown in Fig. 5(a). In this problem, two assumptions are done. Firstly, the disk is much harder than the pin, so its wear is negligible in comparison with the wear suffered by the pin. Secondly, the pin is far enough away from the axis of the disk so that all points in the contact zone have uniform and constant slip velocity and travel the same distance during the wear process. Both bodies have the same Young's modulus and Poisson's ratio values: $E = 210$ GPa and $\nu = 0.3$, respectively. The pin, whose radius is $R = 50$ mm, is sliding on the disk, subjected to a constant normal load $P = 10.2 \, N$.

For the numerical analysis, a quasi-static contact problem can be considered since the formulation assumes that the axes are moving with the contact zone, which is moving with the punch. Therefore, the tangential slip velocity (or the sliding distance) on the contact zone is imposed on the computational domain elements. For the following studies, the sliding direction is the x axis (i.e., $\theta = -\beta$ in Fig. 2(b)).

4.1.1. Pin on disk validation problem

To validate the proposed formulation, we are going to consider first an isotropic wear law, i.e., $i_1 = i_2 = i_w$ with $i_w = 1.33 \cdot 10^{-7}$ MPa^{-1}. The theoretical solution proposed by Hegadekatte et al. in [33] to compute the evolution of the total maximum wear depth (w) on the pin and the total worn volume (W) as a function of the sliding distance (s) can be obtained by solving the worn volume expression for the spherical pin presented in Fig. 5(a): $W = \pi(3R - w)w^2/3$, and the Holm–Archard's law: $W = i_w P \, s$. An alternative analytical solution was proposed by Argatov in [34], where the total maximum wear depth is computed as a function of the semi-contact width (a), as: $w = a^2/2R$, being $a = \sqrt[4]{a_o^4 + 4 \, i_w P \, s \, R/\pi}$ and a_o the initial semi-contact width. The advantage of Argatov's analytical solution is that it also allows us to obtain the maximum contact pressure evolution in the steady-state wear regime: $p_{max} = P/\pi a^2$.

This benchmark problem have been also solved with the numerical scheme presented in this work. The computational domain region size is 1.6 mm × 1.6 mm and considers 81 × 81 mesh elements. The numerical results have been obtained for a sliding distance $s = 640$ mm, being sliding distance increment value of 1 mm.

The theoretical and numerical results of the maximum wear depth evolution on the pin surface, the semi-contact width and the maximum contact pressure evolution, as a function of the sliding distance, are presented in Fig. 6. In Fig. 6(a) is presented the computed maximum wear depth evolution on the pin surface – as a function of the sliding distance – by comparison with the Argatov's analytical solution [34] and the Hegadekatte's semianalytical solution [33]. The evolution of the semi-contact width and the maximum contact pressure value are presented in Fig. 6(b) and (c), respectively, by comparison with Argatov's solution [34]. All the results are non-dimensional. The sliding distance and the contact semi-width are expressed relative to the initial contact semi-width ($a_o = 0.15$ mm). The maximum contact pressure is presented relative to the initial maximum contact pressure (p_o) and the maximum wear depth is expressed relative to the spherical pin
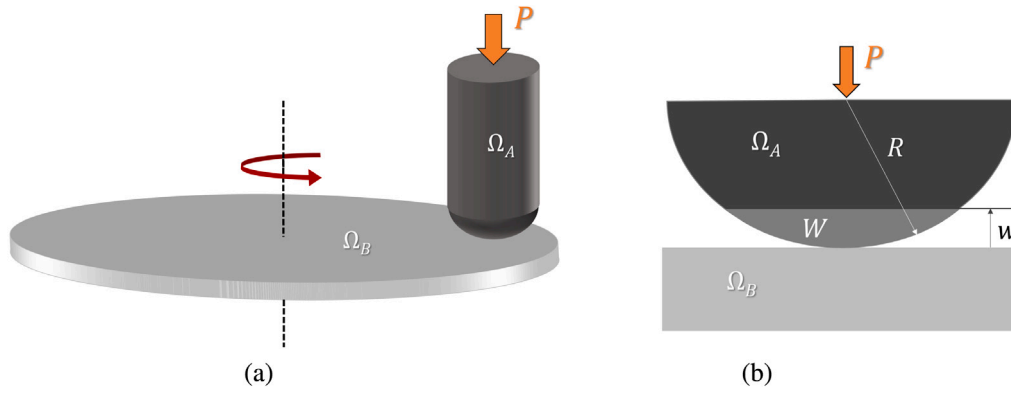
Fig. 5. (a) Schematic diagram of a pin-on-disk sliding contact system. (b) Pin wear volume (W) and pin maximum wear depth (w) due to the action of the normal load P and the sliding distance (s) of the rotating disk.
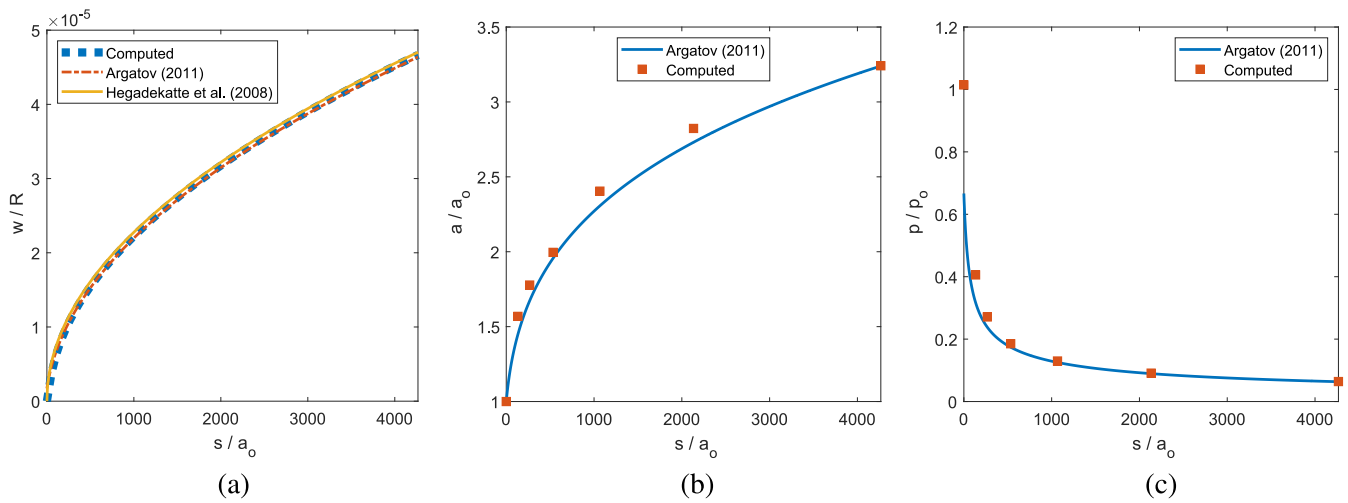

Fig. 6. (a) Computed maximum wear depth evolution on the pin surface as a function of the sliding distance by comparison with the Argatov's analytical solution [34] and the Hegadekatte's semianalytical solution [33]. Evolution of the semi-contact width (b) and the maximum contact pressure value (c) are presented by comparison with Argatov's solution [34]. All the results are non-dimensional: the sliding distance and the contact semi-width are expressed relative to the initial contact semi-width (a_o), the maximum contact pressure is presented relative to the initial maximum contact pressure (p_o) and, finally, the maximum wear depth is expressed relative to the spherical pin radio (R).

radio (R). Numerical results present and excellent agreement with the theoretical solutions.

Similarly, Fig. 7(a) presents the pin profile evolution as a function of the sliding distance, whereas Fig. 7(b) shows the normal contact pressure distributions, as a function of the sliding distance. All the results are non-dimensional. The sliding distance is expressed relative to the initial contact semi-width (a_o), the pin profile is presented relative to the spherical pin radio (R) and the contact pressure distribution is presented relative to initial maximum Hertzian contact pressure (p_o). We can see in Fig. 7(b) how, due to wear evolution, the contact area enlarges and the maximum normal pressure value decreases with respect to the Hertz solutions, a_o and p_o, respectively.

4.1.2. Influence of the friction intensity

After the validation, we study the influence of the friction intensity on the subsurface stress distributions (i.e., the maximum values and the locations) and their evolution caused by the sliding wear. For this purpose, the previous section analyses are now developed considering different values of the friction coefficients: $\mu_1 = \mu_2 = \mu$, being $\mu = \{0, 0.15, 0.25, 0.35, 0.50, 0.65\}$. The resulting Von Mises stress distribution inside the solid – along z axis – is presented in Fig. 8 for every value of μ, as a function of wear evolution, via the accumulated sliding distance (s). On these distributions all the variables are non-dimensional, therefore the sliding distance (s) and the z-axis coordinates are expressed

relative to the initial contact semi-width (a_o) and the Von Mises stress is presented relative to the initial maximum contact pressure (p_o).

Fig. 8(a) presents the frictionless case. The initial Von Mises stress distribution (when $s/a_o = 0$) presents an excellent agreement with the theoretical solution [5]: $\sigma_{VM}/p_o = 0.620$ at $z/a_o = 0.48$. However, due to the sliding wear evolution, the stress maximum value decreases and its location moves to the interior of the solid: $z/a_o > 0.48$. This behavior is more clearly observed in Fig. 19(a) – Appendix D–, where the evolution of the Von Mises stress distributions in the xz plane (for $y = 0$) are presented for different accumulated sliding distances.

The frictional cases are presented in Figs. 8(b–f). Observing the Von Mises stress distributions when $s/a_o = 0$ (black line) on these figures, we can affirm the following: an increase on the friction coefficient value generates an increment in the value of the local maximum Von Mises stress, both beneath and near the surface. Moreover, there is a friction coefficient threshold value (around $\mu = 0.35$) which shifts the location of the principal Von Mises stress value.

The colored lines on Figs. 8 (b–f) show how – depending on the friction intensity – the stress evolves with wear, i.e., reducing its maximum value during the sliding wear process, However, the location in that subsurface stress maximum value depends on the friction coefficient value. When the friction coefficient value is lower than the mentioned friction coefficient threshold, wear increases with the sliding distance and the maximum Von Mises stress location goes deeper into the solid. Contrary, if the friction coefficient is higher than the friction threshold,
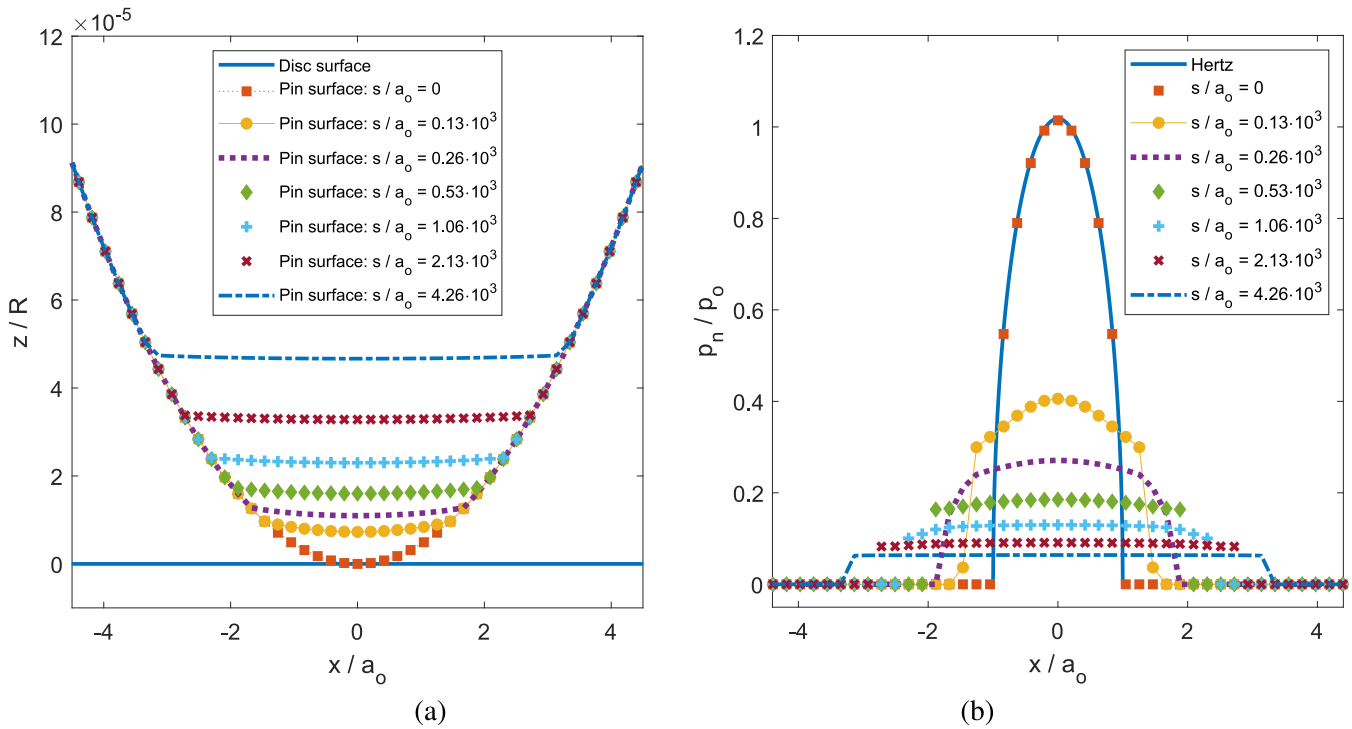
Fig. 7. (a) Pin profile evolution and (b) evolution of the normal contact pressure distributions, as a function of the sliding distance. All the results are non-dimensional: the sliding distance is expressed relative to the initial contact semi-width (a_o), the pin profile is presented relative to the spherical pin radio (R) and the contact pressure distribution is presented relative to initial maximum Hertzian contact pressure (p_o).

wear increases with the sliding distance but, the maximum Von Mises stress prevails on the surface. Thus, under sliding wear conditions, wear reduces Von Mises stress magnitude and shifts the location of the maximum Von Mises stress value ($\sigma_{VM,max}$) inward. However, friction shifts the location of $\sigma_{VM,max}$ to the surface when it is considered in the sliding wear problem.

The effect of both wear and friction can also be appreciated in Fig. 19(a), (b) and (c) – Appendix D– , where the influence of friction on the evolution of the dimensionless Von Mises stress (σ_{VM}/p_o) distributions in the xz plane are shown for: $\mu = 0$, $\mu = 0.25$ and $\mu = 0.50$, respectively. On the one hand, when the figures in Fig. 19 – Appendix D – are compared in the vertical direction, it is possible to recognize the translation of the $\sigma_{VM,max}$ location towards the surface or towards the interior of the material depending on the value of the friction coefficient with respect to the threshold friction value. In column (a), where $\mu = 0$, it is evident how $\sigma_{VM,max}$ location moves inward, whereas in column (c), i.e., for $\mu = 0.50$, the $\sigma_{VM,max}$ location stays at the surface. On the other hand, when figures in Fig. 19 – Appendix D – are compared horizontally, it can be detected how as the friction increases, Von Mises stress also increases its magnitude while it moves away from the center of the solid and becomes shallower.

Finally, Fig. 9(a) presents the evolution of the maximum value of dimensionless Von Mises stress ($\sigma_{VM,max}/p_o$) and its z and x location (see Figs. 9 (b) and (c), respectively), as a function of the non dimensional sliding distance (s/a_o) and several values of the friction coefficient. We can observe how, for the frictionless case, the $\sigma_{VM,max}$ is located at the interior of the solid and remains on the z axis. For slightly friction intensity values, the location of the $\sigma_{VM,max}$ location remains at the interior of the solid during the running in sliding wear regime, but at certain sliding distance, it shifts to the surface. There is a friction coefficient threshold value (around $\mu = 0.35$) above which the $\sigma_{VM,max}$ location remains on the surface during all the sliding wear process.

4.1.3. Influence of the sliding direction under orthotropic friction and wear laws

Now this problem is studied under orthotropic friction and wear laws (i.e, under $\mu_1 \neq \mu_2$ and $i_1 \neq i_2$). Therefore, we study the influence

of the sliding direction angle relative to the tribological principal axes (i.e., θ, according to Fig. 2(b)). Due to the sliding direction is fixed to be parallel to the x-axis, the θ angle is set to $\theta = -\beta$, being β the tribological axes angle orientations. In this example, we are going to consider several values for the orientation angle β, i.e, $\beta = \{0°, 45°, 90°\}$. The orthotropic friction principal direction coefficients values are: $\mu_1 = 0.25$ and $\mu_2 = 0.50$, i.e., $\mu_1 < 0.35$ and $\mu_2 > 0.35$ (being 0.35 the friction coefficient threshold value computed in Section 4.1.2). The corresponding wear coefficients values are: $i_1 = 1.33 \cdot 10^{-7}$ and $i_2 = 2.66 \cdot 10^{-7}$ MPa^{-1}. Under this choice of the friction and wear coefficient values, the effective friction and wear coefficient values are β angle dependent, i.e, they have been set to increase their values as the β angle increases.

Fig. 10 shows the influence of β on the wear variables. Fig. 10(a) presents the computed maximum wear depth evolution on the pin surface under orthotropic friction and wear conditions ($i_2 = 2i_1$) and different values of the tribological axes angle orientations: $\beta = \{0°, 45°, 90°\}$. The computed results are validated by comparison with the Argatov's analytical solution [34] for $i_w = i_w(\theta)$ (being $\theta = -\beta$). Fig. 10(b) shows the total wear volume on the pin as a function of the sliding distance, for different values of the tribological axes angle orientations (β), being the wear volume (W) presented relative to the hemisphere volume with the same radio of the pin ($W_o = 2 \pi R^3/3$). It is clear the influence of β on the severity of wear.

It is important to emphasize the importance of considering orthotropic friction and wear laws, since, although the solution for $\beta = 0°$ or $\beta = 90°$ could be also obtained solving an isotropic problem with $\mu = \mu_1$ and $i_w = i_1$ or $\mu = \mu_2$ and $i_w = i_2$, respectively, due to the highly no linearity of this problem, the solution for $\beta = 45°$ could not be computed as the mean value between the solutions for $\beta = 0°$ and $\beta = 90°$. Or in other words, the difference between the accumulated wear depth (or wear volume) presented in Fig. 10 for $\beta = 90°$ and $\beta = 0°$ is not the double of the difference between the accumulated wear for $\beta = 45°$ and $\beta = 0°$, although $i_1 = 2i_2$.

Fig. 11 shows evolution of the normal pressure distributions computed assuming an isotropic tribological laws and orthotropic friction
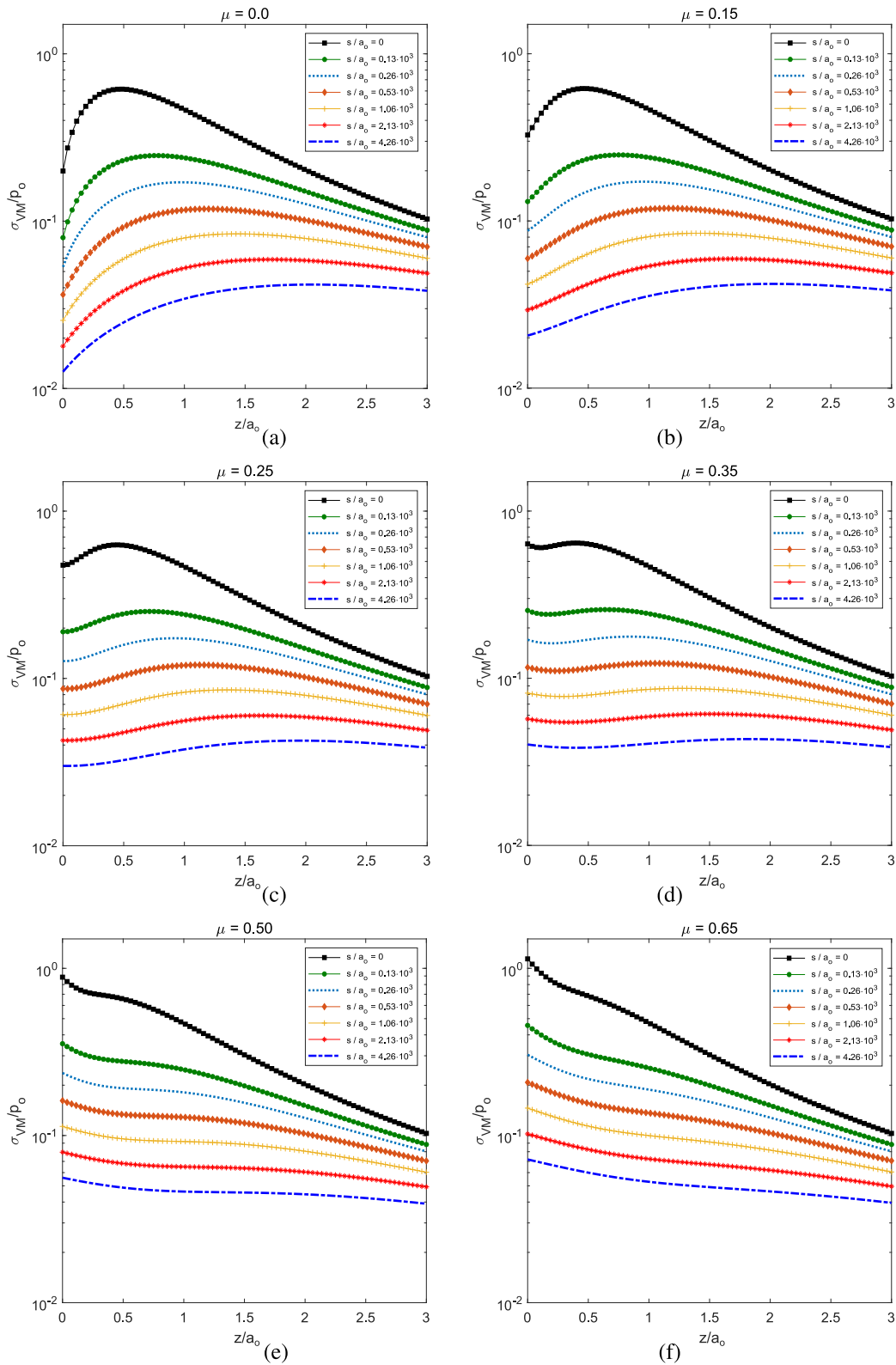
Fig. 8. Influence of friction on the evolution of the z-axis Von Mises stress distributions for the accumulated sliding distance (s). All the variables are non-dimensional: the sliding distance (s) and the z-axis coordinates are expressed relative to the initial contact semi-width (a_o) and the Von Mises stress is presented relative to the initial maximum contact pressure (p_o).

and wear laws, for the sliding distances: (a) $s/a_o = 20/3$ (b) $s/a_o = 400/3$ (c) $s/a_o = 1600/3$. Different values of the tribological axes angle orientations, i.e., $\beta = \{0°, 45°, 90°\}$, have been considered to show how the sliding direction angle relative to the tribological principal

axes ($\theta = -\beta$) also affects on the normal pressure distribution and contact area. In Fig. 11, we observe important discrepancies on the maximum normal pressure evolution obtained for $\beta = \{0°, 45°, 90°\}$. Similar discrepancies are observed on the contact area evolution.
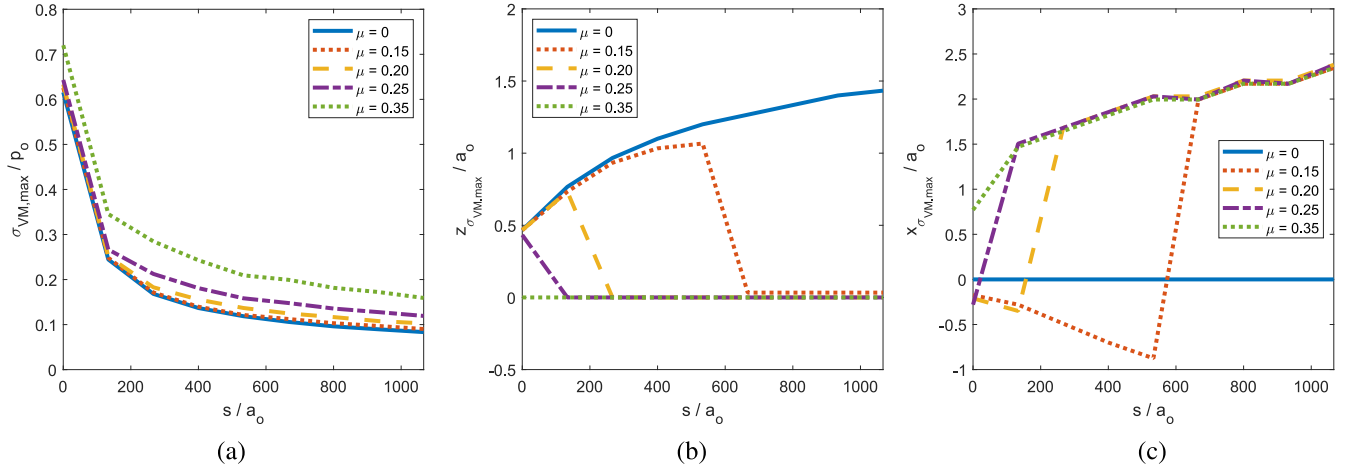
Fig. 9. Evolution of the maximum value of dimensionless Von Mises stress ($\sigma_{VM,max}/p_o$) (a) and its locations, i.e., (b) z location and (c) x location, as a function of the non dimensional sliding distance (s/a_o) and several values of the friction coefficient.
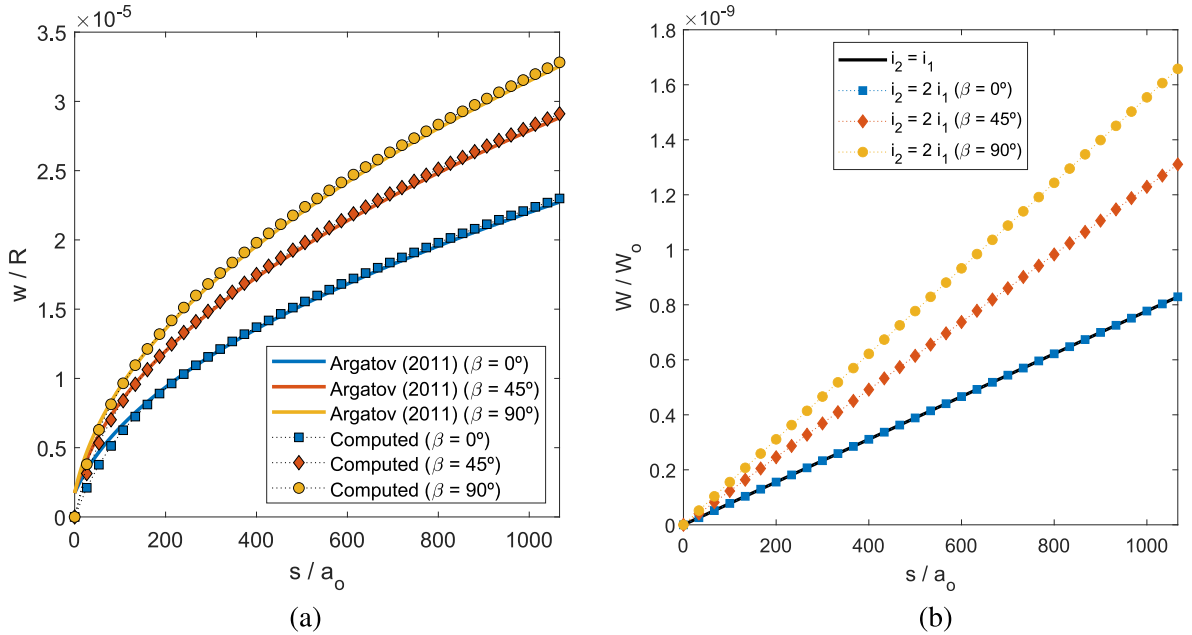

Fig. 10. (a) Computed maximum wear depth evolution on the pin surface under orthotropic friction and wear conditions ($i_1 = 2i_2$) and different values of the tribological axes angle orientations: $\beta = \{0°, 45°, 90°\}$. The computed results are presented by comparison with the Argatov's analytical solution [34] for $i_w = i_w(\theta)$ (being $\theta = -\beta$). (b) Computed total wear volume on the pin as a function of the sliding distance, for different values of the tribological axes angle orientations (β), being the wear volume (W) presented relative to the hemisphere volume with the same radio of the pin ($W_o = 2 \pi R^3/3$).

However, the main discrepancies are observed on the subsurface stress distributions. The xz plane stress distributions are presented in Fig. 12 and the yz plane stress distributions are showed in Fig. 20 — Appendix E. These figures show the influence of the sliding direction angle relative to the tribological principal axes (i.e., $\theta = -\beta$) on the evolution of the dimensionless Von Mises stress (σ_{VM}/p_o) distributions caused by wear. Figs. 12(a), (b) and (c) present the evolution of σ_{VM}/p_o distributions for $\beta = 0°$, $\beta = 45°$ and $\beta = 90°$, respectively. On these figures, it is possible to recognize a behavior similar to that commented in Fig. 8, i.e., the stress evolves, reducing its maximum value during the sliding wear process. Moreover, the location of the maximum value of Von Mises stress goes deeper into the solid when the sliding distance increases. However, comparing Figs. 12(a), (b) and (c) for a fixed sliding distance, we can observe how the value of the maximum Von Mises stress increases its magnitude with the angle β while its location moves to the surface.

Finally, the stress distributions in the yz plane (see Fig. 20) – Appendix E – reveal the same behavior, but they are even more affected by the orthotropic friction law in the following way. Although xz plane is a plane of symmetry for the geometry of the problem and its loads, Fig. 20(b) shows a non-symmetric solution for the stress distribution. This is due to the fact that we are considering an associated sliding rule, so the direction of tangential contact traction can be different from the slip direction, i.e.,

$$\frac{p_{e_2}}{p_{e_1}} = \left(\frac{\mu_2}{\mu_1}\right)^2 \frac{\dot{g}_{e_2}}{\dot{g}_{e_1}} \tag{38}$$

according to the orthotropic friction law, but maximizing the rate of energy dissipation for those contact points on sliding state [68]. Consequently, although the pin is sliding on x direction, non zero tangential traction components p_x and p_y are obtained for the $\beta = 45°$ case. Figs. 13 (a) and (b) show the quiver plots of the tangential contact traction vectors ($\mathbf{p}_t$) and the tangential slip vectors ($\dot{\mathbf{g}}_t$) for
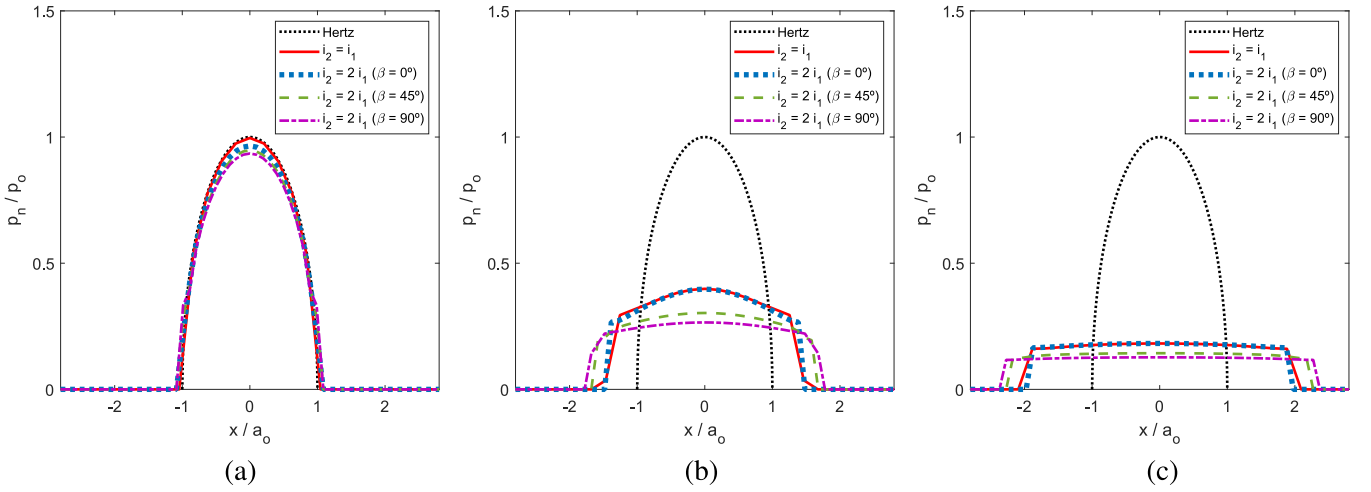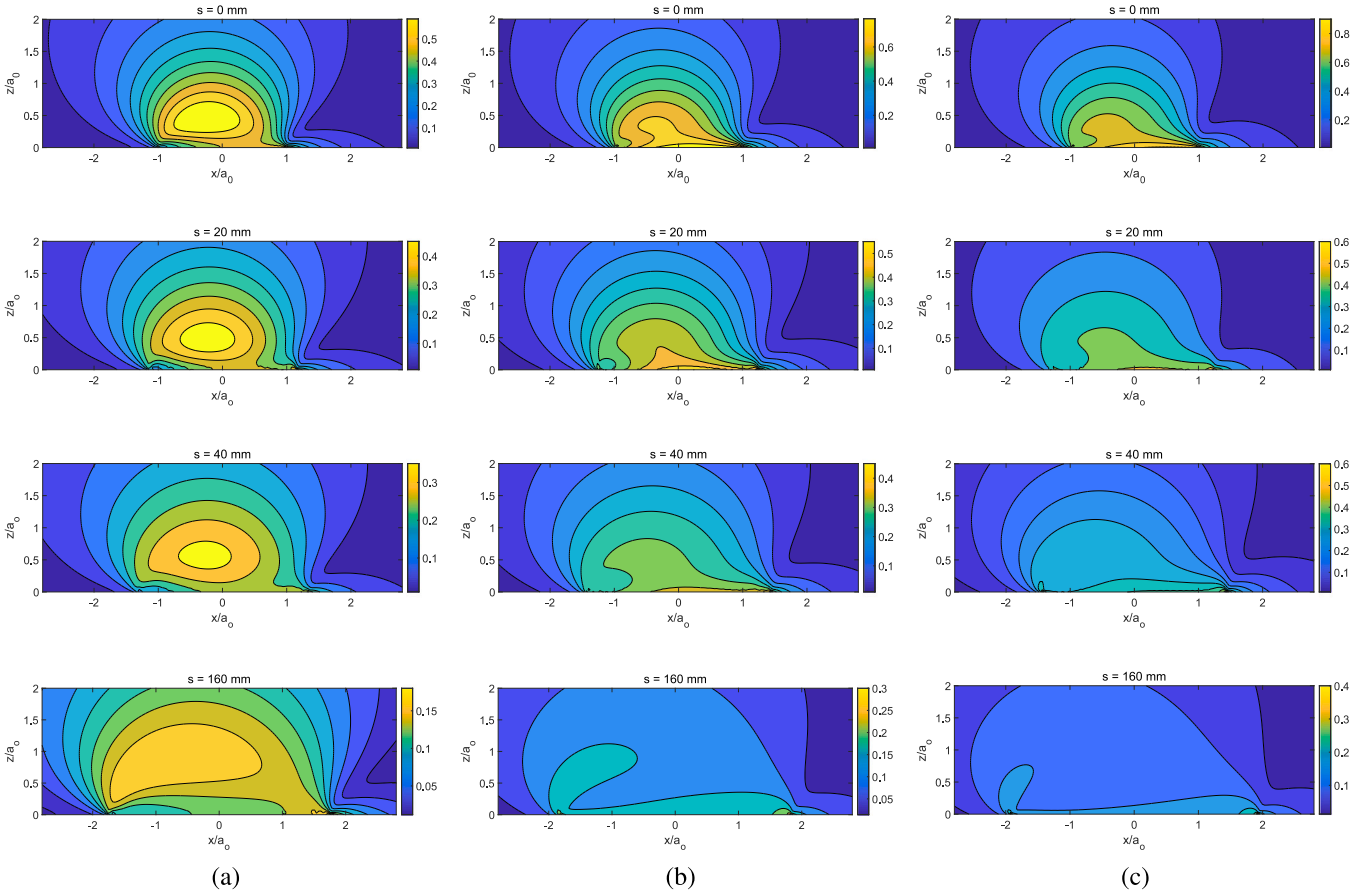
Fig. 11. Normal pressure distributions computed assuming an isotropic tribological laws and orthotropic friction and wear laws, under different values of the tribological axes angle orientations: $\beta = \{0°, 45°, 90°\}$, for the sliding distances: (a) $s/a_o = 20/3$ (b) $s/a_o = 400/3$ (c) $s/a_o = 1600/3$.

Fig. 12. Influence of the sliding direction angle relative to the tribological principal axes (i.e., $\theta = -\beta$) on the evolution of the dimensionless Von Mises stress (σ_{VM}/p_o) distributions in the xz plane for: (a) $\beta = 0°$, (b) $\beta = 45°$ and (c) $\beta = 90°$, and the nondimensional sliding distances: $s/a_o = 0$, $s/a_o = 20/3$, $s/a_o = 800/3$ and $s/a_o = 3200/3$. The x and z coordinates are expressed relative to the initial contact semi-width ($a_o = 0.15$ mm).

sliding distances: $s/a_o = 20/3$ and $s/a_o = 400/3$, respectively. In these figures we can observe how the components of $\mathbf{p}_t$ and $\dot{\mathbf{g}}_t$ expressed in the tribological axes follow the relation presented in Eq. (38).

4.2. Subsurface stress evolution under fretting wear

This section studies the evolution of the subsurface stresses when the solids in contact are subjected to – orthotropic – fretting wear

conditions. In this case, a sphere, whose radius is $R = 50$ mm (see Fig. 14), is subjected to a normal indentation $g_{n,o} = 0.008$ mm over an elastic half-space and to a repeated alternating tangential displacement in the x-direction, whose amplitude is 0.004 mm. Both bodies have the same Young's modulus value $E = 210$ GPa and the same Poisson's ratio value $v = 0.3$. The computational contact domain considers 61×61 mesh elements, being the surface region size: $1.6 \text{ mm} \times 1.6 \text{ mm}$. The influence of the sliding direction angle relative to the tribologi-
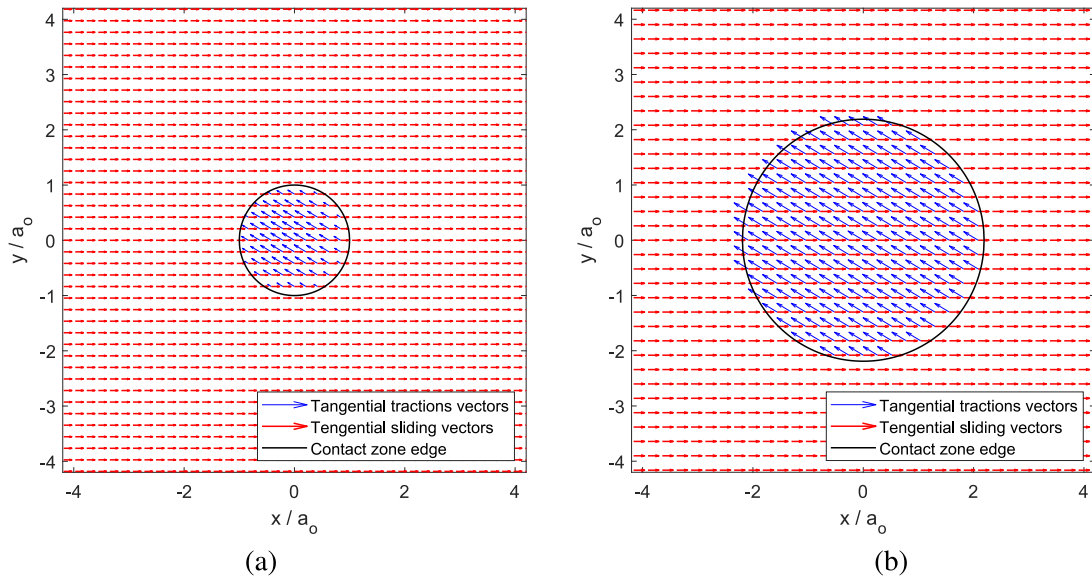
Fig. 13. Quiver plots of the tangential contact traction vectors ($\mathbf{p}_t$) and the tangential slip vectors ($\dot{\mathbf{g}}_t$) for: (a) $s/a_o = 20/3$ and (b) $s/a_o = 400/3$. The components of $\mathbf{p}_t$ and $\dot{\mathbf{g}}_t$ expressed in the tribological axes follow the relation presented in Eq. (38).
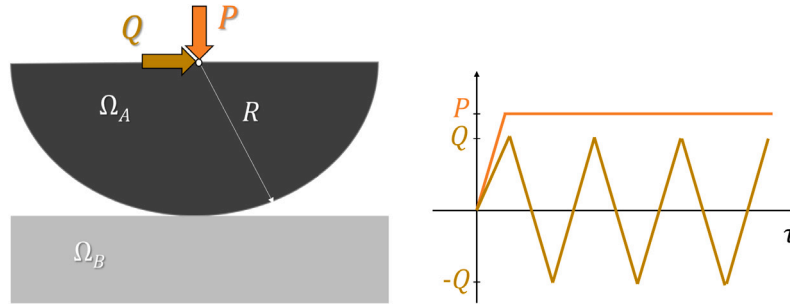

Fig. 14. Spherical punch over an elastic half-space under fretting wear conditions.

principal axes (i.e., $\theta = -\beta$) on the evolution of the dimensionless Von Mises stress (σ_{VM}/p_o) is again studied but, this time, under fretting wear conditions. For this purpose, we are going to consider several values for the orientation angle β, i.e, $\beta \in [0°, 90°]$. The orthotropic friction principal direction coefficient values are: $\mu_1 = 0.1$ and $\mu_2 = 0.65$, respectively, and the corresponding wear coefficients are: $i_1 = 1.33 \cdot 10^{-7}$ MPa^{-1} and $i_2 = 8.645 \cdot 10^{-7}$ MPa^{-1}.

The total wear depth computed after $N = \{10^2, 10^4, 10^5\}$ cycles is presented in Figs. 15 (a), (b) and (c), respectively, for the β values: $\beta = \{0°, 60°, 70°, 80°, 90°\}$. Results reveal that, depending on the value of β, the spherical punch can be subjected to gross slip or partial slip fretting wear conditions. For instance, for $\beta = 0°$, the wear increases widening the contact zone under gross slip conditions. Contrary, for $\beta = 90°$, the partial slip behavior leads to a kind of concentric crown wear depth distribution, where the interior surface points remain in adhesion with no possibility to get worn.

Due to that resulting surface damage (i.e., wear depth), the evolution of the solids profiles present different shapes with the number of cycles. The resulting solids profile evolution in the xz plane under fretting wear conditions for $\beta = 30°$ is presented in Fig. 16(a), whereas 16 (b) shows the resulting solids profiles evolution for $\beta = 90°$. In the first case the evolution of the solids profiles adopt a gross slip distribution and, in the second case, the evolution of the solids present a partial slip distribution. In both cases, the resulting wear profiles have been computed considering that the surface hardness of the plane is twice the surface hardness of the spherical punch.

The evolution of the resulting normal pressure distributions for $\beta = 30°$ are presented in Fig. 17(a) and, in Fig. 17(b), we can see

the normal pressure distributions for $\beta = 90°$. It can be noted that for low cycles of operation, there are no differences with the Hertz normal pressure. However, while accumulating cycles of operation, the pressure distributions evolves to different shapes. In the case of gross slip behavior, Fig. 17(a) shows how the pressure decreases while the contact zone increases. Contrary, when a partial slip behavior prevails, Fig. 17(b) reveals that the normal contact pressure evolves from an Hertzian distribution to a close complete normal contact traction distribution over the stick zone, being its maximum values developed more than two times greater than the maximum in the first cycles.

The differences observed in the evolution of the surface contact pressures caused by the β angle lead to different subsurface stress distributions. In Appendix F, Figs. 21 (a–c) present the evolution of the dimensionless Von Mises stress (σ_{VM}/p_o) distributions in the xz plane after $N = \{10^2, 10^4, 10^5\}$ cycles, respectively, for the tribological axes orientation angle values: $\beta = \{0°, 60°, 70°, 80°, 90°\}$. On these figures, we can see how the maximum value of the Von Mises stress ($\sigma_{VM,max}$) and its location is clearly affected not only by the number of cycles, but also by the β angle.

The results presented reveal the tremendous influence of the sliding direction angle – relative to the tribological principal axes – (i.e., $\theta = -\beta$, in this example) in the fretting wear problem, when orthotropic friction and wear conditions are considered. Its value controls not only the friction and wear intensity, but also the fretting wear regime, the surface contact tractions and the subsurface stress distributions.

To point out the influence of the β angle on the evolution of the subsurface stresses, we present Fig. 18. In Fig. 18(a), we show the
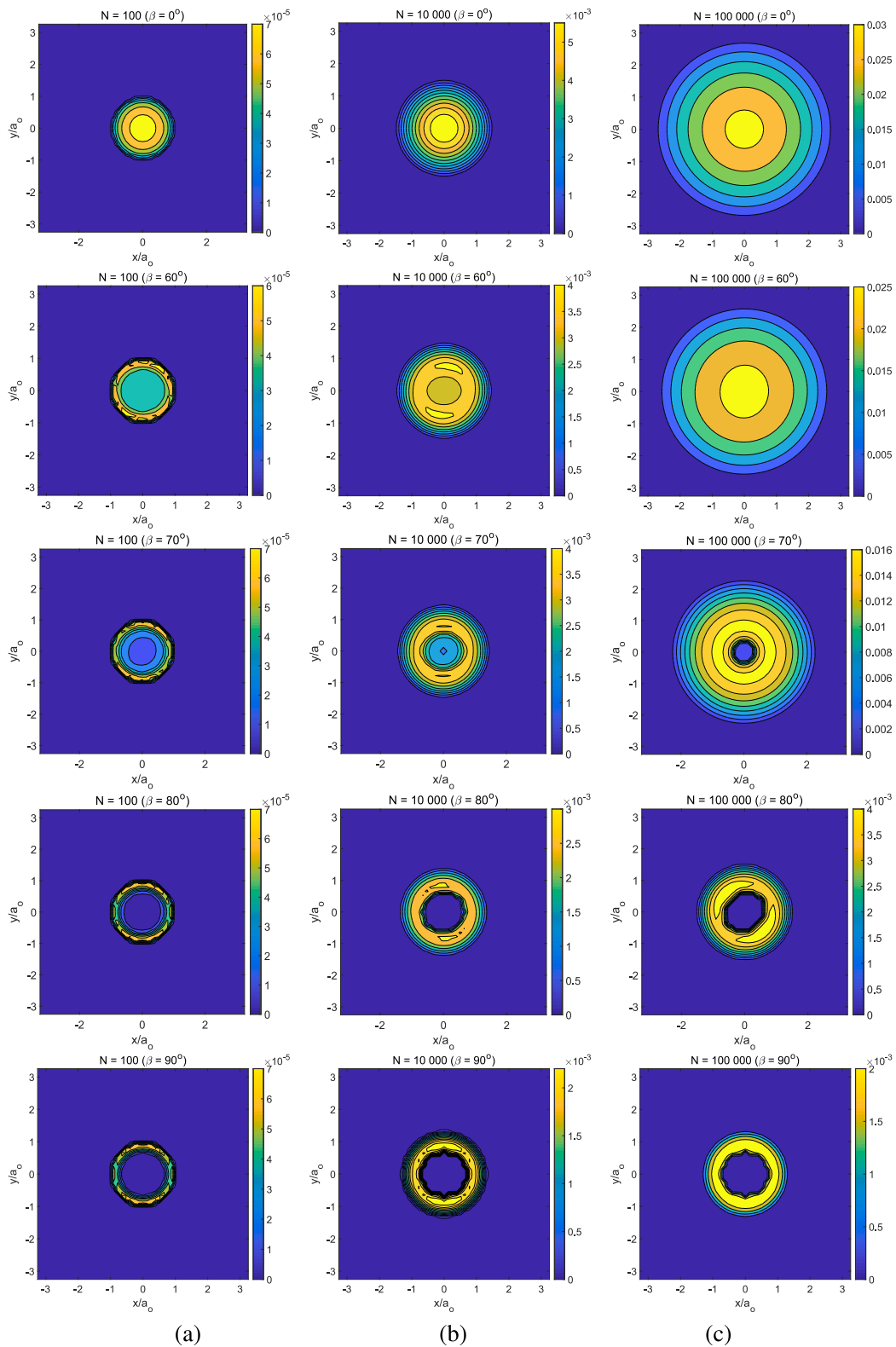
Fig. 15. Influence of the sliding direction angle relative to the tribological principal axes (i.e., $\theta = -\beta$) on the resulting wear depth distribution after: (a) $N = 10^2$ cycles, (b) $N = 10^4$ cycles and (c) $N = 10^5$ cycles. In this figure, the considered values of β angle are: $\beta = \{0°, 60°, 70°, 80°, 90°\}$.

maximum value of the dimensionless Von Mises stress ($\sigma_{VM,max}/p_o$) as a function of the β angle for $N = \{10^2, 10^4, 10^5\}$ cycles. It is interesting to observe in Figs. 18 (a) that there is a threshold value for the β angle (i.e., $\beta \approx 67°$) where the fretting wear regime moves from *gross slip* to *partial slip* regime. These conclusions can be achieved by observing

the computed wear depth in Fig. 15. Moreover, for that threshold value ($\beta = 67°$) we observe the maximum values for $\sigma_{VM,max}$ when the steady state fretting wear regime is reached (i.e., $N = 10^5$ cycles) . Finally, it is also interesting to observe in Fig. 18(b) the influence of the β angle in the z location of these $\sigma_{VM,max}$ values after $N = \{10^2, 10^4, 10^5\}$ cycles.
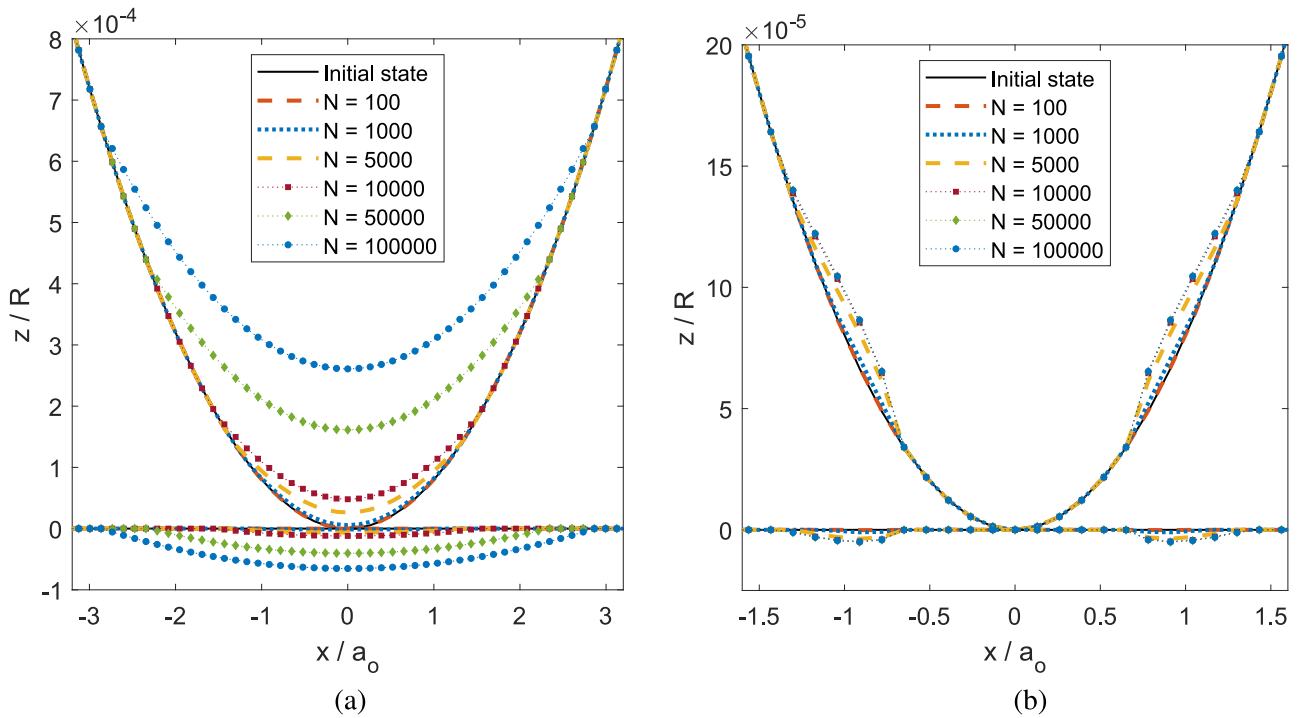
Fig. 16. Solids profiles evolution in the xz plane under fretting wear conditions for: (a) $\beta = 30°$ (which results in gross slip conditions) and (b) for $\beta = 90°$ (which results in partial slip conditions).

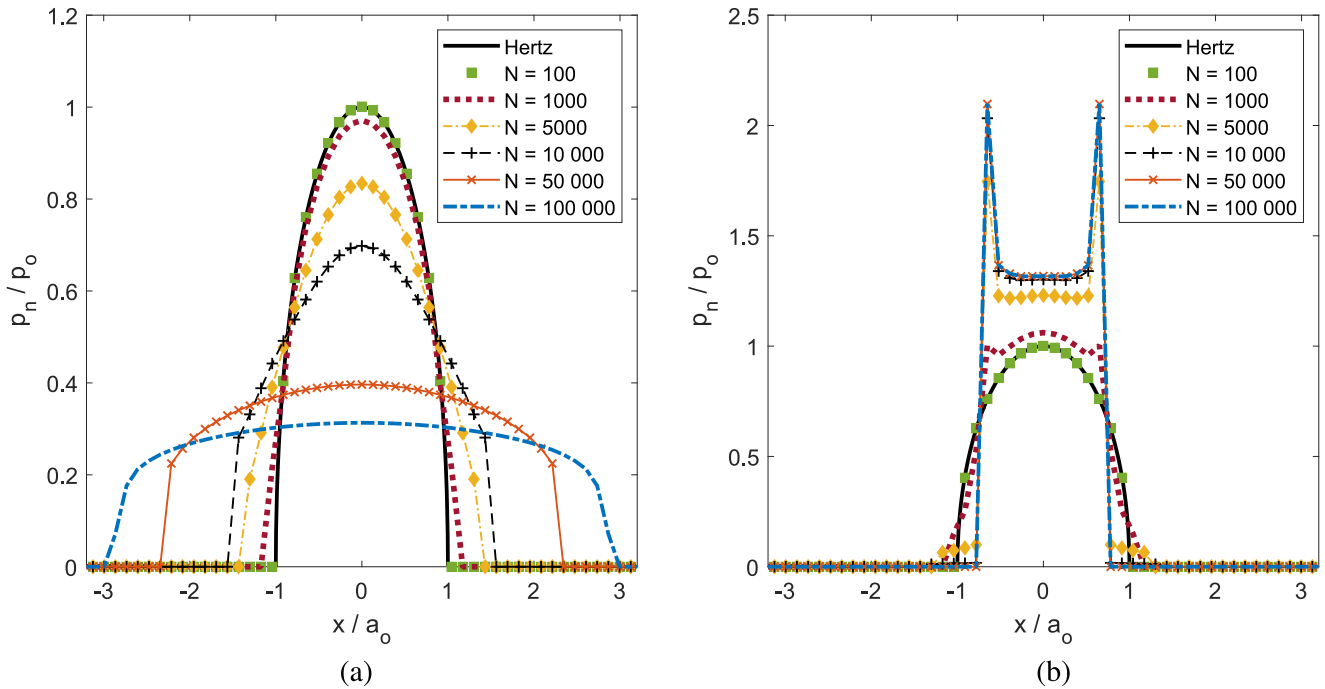**Fig. 17.** Normal contact pressure evolution in the xz plane under fretting wear conditions for: (a) $\beta = 30°$ and (b) for $\beta = 90°$.

In general, the location of the $\sigma_{VM,max}$ moves to the surface (or remain on the surface) with the number of cycles. However, for some values of the β angle (i.e., $\beta \approx 0°$ or $\beta \in [50°, 70°]$), the $\sigma_{VM,max}$ location moves inward with the number of cycles.

5. Resume and conclusions

This paper presents an influence coefficient formulation and a solution scheme to study the evolution of the subsurface stresses in contacting solids under orthotropic sliding wear and fretting wear conditions. This computational framework has been applied to study how the values of the orthotropic friction and wear coefficients, and the sliding direction – relative to the tribological axes – affect the wear regime and the evolution of the solids profiles, the surface contact tractions and, primarily, the subsurface – Von Mises – stress: distribution, maximum value and subsurface location, during the wear process.

Firstly, we solved a benchmark sliding wear contact problem (i.e., a pin-on-disk problem). The maximum wear depth evolution,
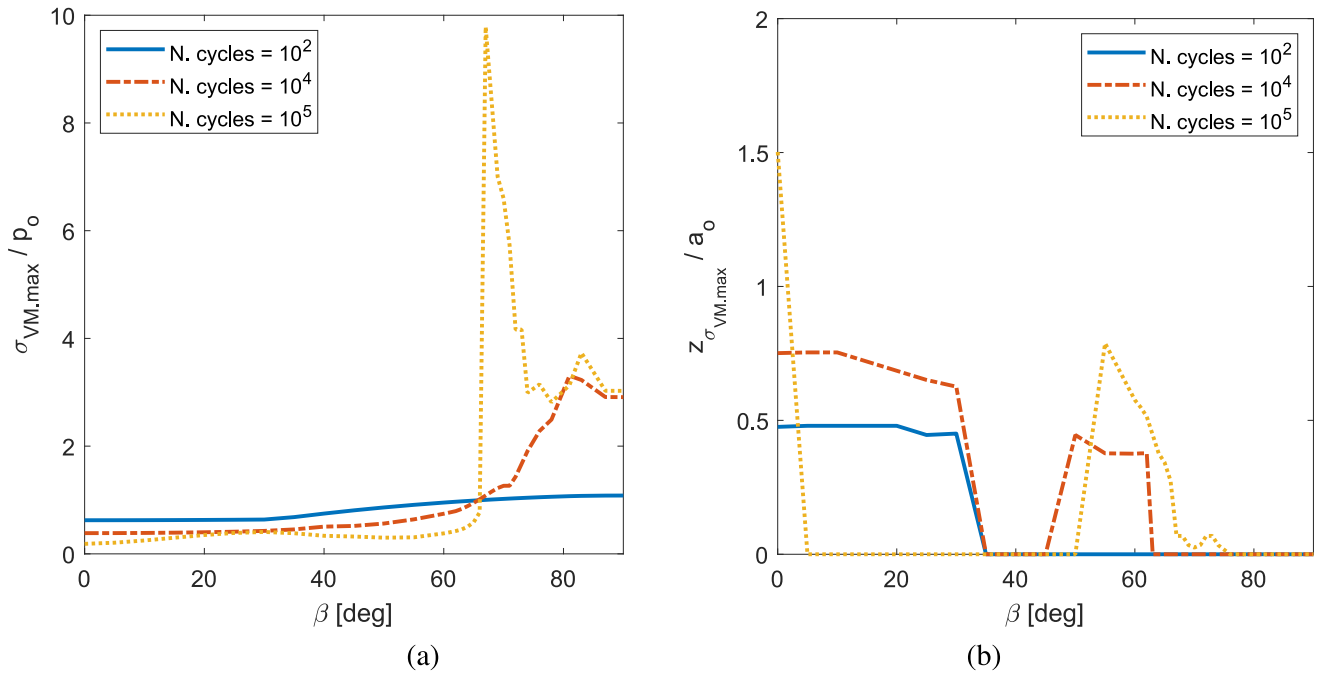
Fig. 18. (a) Influence of the sliding direction in the maximum value of the dimensionless subsurface Von Mises stress ($\sigma_{VM,max}/p_o$) for $N = \{10^2, 10^4, 10^5\}$ cycles. (b) Influence of the sliding direction in the z location of these maximum values of the subsurface Von Mises stress after N cycles.

semi-contact width and maximum contact pressure evolution were computed as a function of the sliding distance, and successfully validated by comparison with the analytical solutions presented by Argatov in [34].

Secondly, the influence of the friction intensity on the subsurface stress distributions (i.e., maximum value of Von Mises stress – $\sigma_{VM,max}$ – and its location), as well as their evolution caused by the – isotropic – sliding wear, were studied. The results presented in Fig. 9 allow us to say that, during the sliding wear process, the subsurface stress evolves reducing its maximum value. However the location of $\sigma_{VM,max}$ depends on the intensity of friction. For the frictionless case, the $\sigma_{VM,max}$ is located at the interior of the solid and goes deeper into the solid when the sliding distance increases. However, for slightly friction intensity values, the location of the $\sigma_{VM,max}$ remains at the interior of the solid during the running in sliding wear regime, but at certain sliding distance, it shifts to the surface. Moreover, there is a friction coefficient threshold value ($\mu \approx 0.35$) above which $\sigma_{VM,max}$ location remains on the surface during all the sliding wear process.

Thirdly, we moved on to the study of the sliding wear problem under orthotropic friction and wear laws. In this case, we studied the influence of the sliding direction relative to the tribological principal axes (i.e., θ, according to Fig. 2(b)). In all these analyses, the sliding direction was fixed to be parallel to x axis and the values of the orthotropic friction principal direction coefficients were set to be $\mu_2 = 2\,\mu_1$, with $\mu_1 < 0.35$ and $\mu_2 > 0.35$ (i.e., 0.35 being the friction coefficient threshold value computed in Section 4.1.2), and the corresponding wear coefficients values to be: $i_2 = 2\,i_1$. Under this election of these coefficient values, the effective friction and wear coefficients increased their values with the β angle. As a consequence, in Fig. 11, we observed important discrepancies on the maximum normal pressure (and on the contact area) evolution when the following values β angle were considered: $\beta = \{0°, 45°, 90°\}$. However, the main discrepancies were observed on the subsurface stress distributions. On the figures presented in Fig. 12, we could recognize a behavior similar to that commented in the isotropic sliding wear problem: the stress evolves reducing its maximum value during the sliding wear process. Moreover, the location of the maximum value of Von Mises stress ($\sigma_{VM,max}$) goes deeper in the solid when the sliding distance increases. However,

comparing Figs. 12(a), (b) and (c) for a fixed sliding distance, we observed that the $\sigma_{VM,max}$ increased its magnitude with the angle β while its location moved to the surface.

Fourthly, to conclude this work, we analyzed the evolution of the subsurface stresses when the solids in contact were subjected to – orthotropic – fretting wear conditions. The results presented in Section 4.2 revealed the tremendous influence of the tribological axes orientation angle – relative to the sliding direction – (i.e., $\theta = -\beta$) in the fretting wear problem, when orthotropic friction and wear conditions are considered. Its value controls not only the friction and wear intensity, but also the fretting wear regime (*gross slip* or *gross slip*), the surface contact tractions and, particularly, the subsurface stress values. We could observe in Figs. 18 how there is a threshold value for the β angle (i.e., $\beta \approx 67°$) where the fretting wear regime moves from *gross slip* to *partial slip* regime. Additionally, for $\beta \approx 67°$, we observed the maximum values for $\sigma_{VM,max}$ when the steady state fretting wear regime was reached (i.e., after $N = 10^5$ cycles).

Finally, to sum up the conclusions of the previous studies, the subsurface stress distribution (i.e. maximum value and its location) – and its evolution – caused by orthotropic wear conditions have showed to be highly depended not only on the friction coefficient values but also on the sliding direction angle — relative to the tribological axes. In other case, we could over- or underestimate their values, having, for instance, important consequences in the fretting fatigue life estimations. Therefore, these aspects need to be considered in the development of more accurate and efficient computational frameworks to estimate wear and to allow engineers to design more efficient mechanical elements.

Declaration of competing interest

The authors declare that they have no known competing financial interests or personal relationships that could have appeared to influence the work reported in this paper.

Data availability

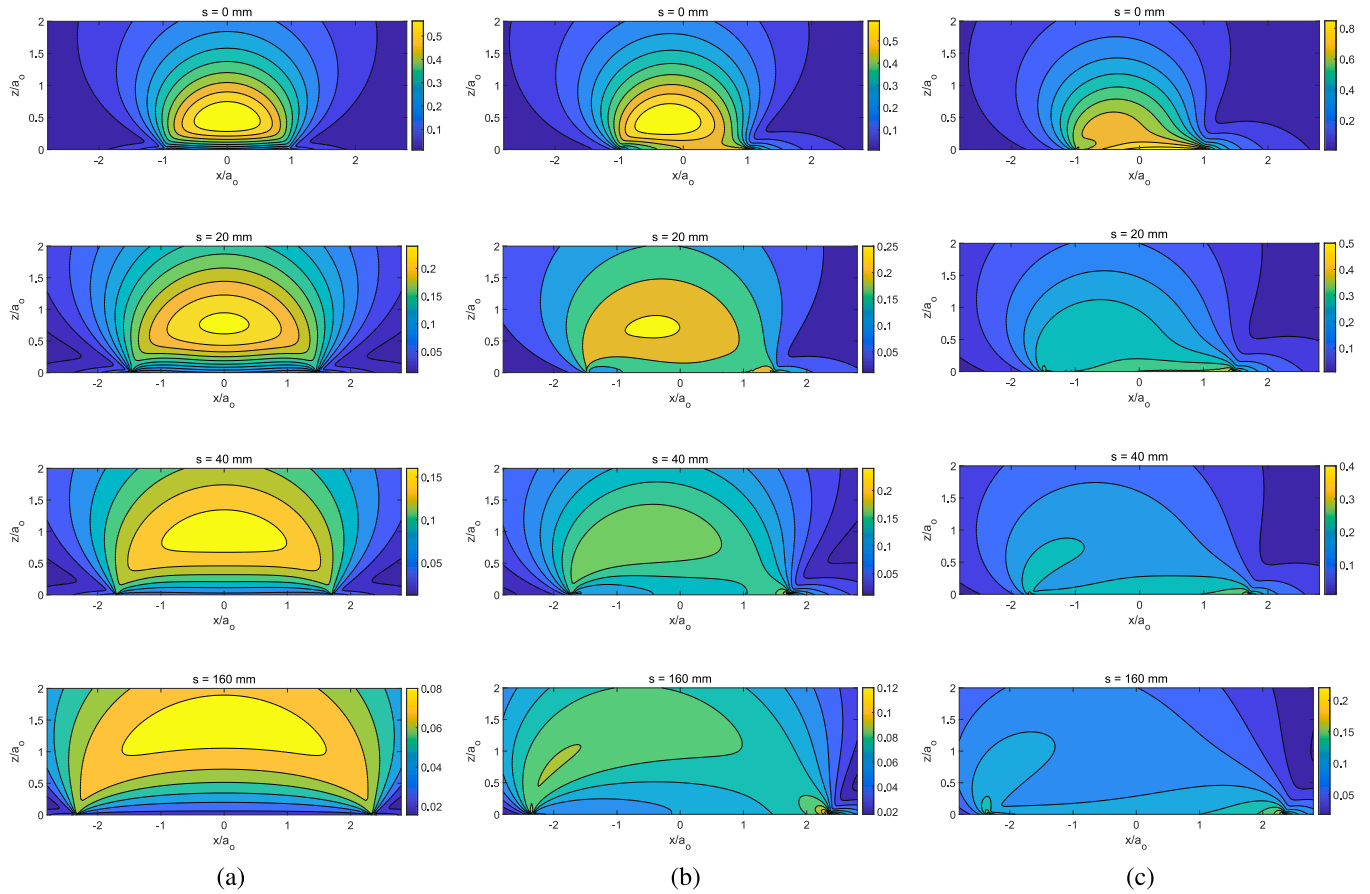Data will be made available on request.

Fig. 19. Influence of friction on the evolution of the dimensionless Von Mises stress (σ_{VM}/p_o) distributions in the xz plane for: (a) $\mu = 0.0$, (b) $\mu = 0.25$ and (c) $\mu = 0.50$.

Appendix A. Subsurface stresses for a unit surface load

The expressions presented below can be found in Johnson's book [5] and give the subsurface stresses due to a unit load applied at the surface origin of a half space Ω^α ($\alpha = A, B$). Therefore, the stress solutions due to a unit normal force at the surface origin of a half space are:

$$T_{xx}^N(x, y, z) = \frac{1}{2\pi}\left[\frac{1 - 2\nu^{(\alpha)}}{r^2}\left[\left(1 - \frac{z}{\rho}\right)\frac{x^2 - y^2}{r^2} + \frac{zy^2}{\rho^3}\right] - \frac{3zx^2}{\rho^5}\right],$$

$$T_{yy}^N(x, y, z) = T_{xx}^N(y, x, z),$$

$$T_{zz}^N(x, y, z) = -\frac{3}{2\pi}\frac{z^3}{\rho^5},$$

$$T_{xy}^N(x, y, z) = \frac{1}{2\pi}\left[\frac{1 - 2\nu^{(\alpha)}}{r^2}\left[\left(1 - \frac{z}{\rho}\right)\frac{xy}{r^2} - \frac{xyz}{\rho^3}\right] - \frac{3xyz}{\rho^5}\right],$$

$$T_{xz}^N(x, y, z) = -\frac{3}{2\pi}\frac{xz^2}{\rho^5},$$

$$T_{yz}^N(x, y, z) = T_{xz}^N(y, x, z),$$

$$(39)$$

where $r = \sqrt{x^2 + y^2}$ and $\rho = \sqrt{x^2 + y^2 + z^2}$.

The stress solutions due to a unit shear force along the x axis at the surface origin of a half space are:

$$T_{xx}^{Sx}(x, y, z) = \frac{1}{2\pi}\left[-\frac{3x^3}{\rho^5} + \left(1 - 2\nu^{(\alpha)}\right)\left[\frac{x}{\rho^3} - \frac{3x}{\rho(\rho + z)^2} + \frac{x^3}{\rho^3(\rho + z)^2}\right.\right.$$
$$\left.\left. + \frac{2x^3}{\rho^2(\rho + z)^3}\right]\right],$$

$$T_{yy}^{Sx}(x, y, z) = \frac{1}{2\pi}\left[-\frac{3xy^2}{\rho^5} + \left(1 - 2\nu^{(\alpha)}\right)\left[\frac{x}{\rho^3} - \frac{x}{\rho(\rho + z)^2} + \frac{xy^2}{\rho^3(\rho + z)^2}\right.\right.$$
$$\left.\left. + \frac{2xy^2}{\rho^2(\rho + z)^3}\right]\right],$$

$$T_{zz}^{Sx}(x, y, z) = -\frac{3}{2\pi}\frac{xz^2}{\rho^5},$$

$$T_{xy}^{Sx}(x, y, z) = \frac{1}{2\pi}\left[-\frac{3x^2y}{\rho^5} + \left(1 - 2\nu^{(\alpha)}\right)\left[-\frac{y}{\rho(\rho + z)^2} + \frac{x^2y}{\rho^3(\rho + z)^2}\right.\right.$$
$$\left.\left. + \frac{2x^2y}{\rho^2(\rho + z)^3}\right]\right],$$

$$T_{xz}^{Sx}(x, y, z) = -\frac{3}{2\pi}\frac{x^2z}{\rho^5},$$

$$T_{yz}^{Sx}(x, y, z) = -\frac{3}{2\pi}\frac{xyz}{\rho^5}.$$

$$(40)$$

Finally, the stress solutions due to a unit shear force along the y axis at the surface origin of a half space can be obtained exchanging x and y in the subscripts and the coordinates of $T_{ij}^{Sx}(x, y, z)$, i.e., $T_{ij}^{Sy}(x, y, z) = T_{ij}^{Sx}(y, x, z)$.

Appendix B. Explicit expression of the surface contact influence coefficients

The explicit expressions of the influence coefficients A_{IJij}, defined in Section 3.1, can be presented, according to [15], as:
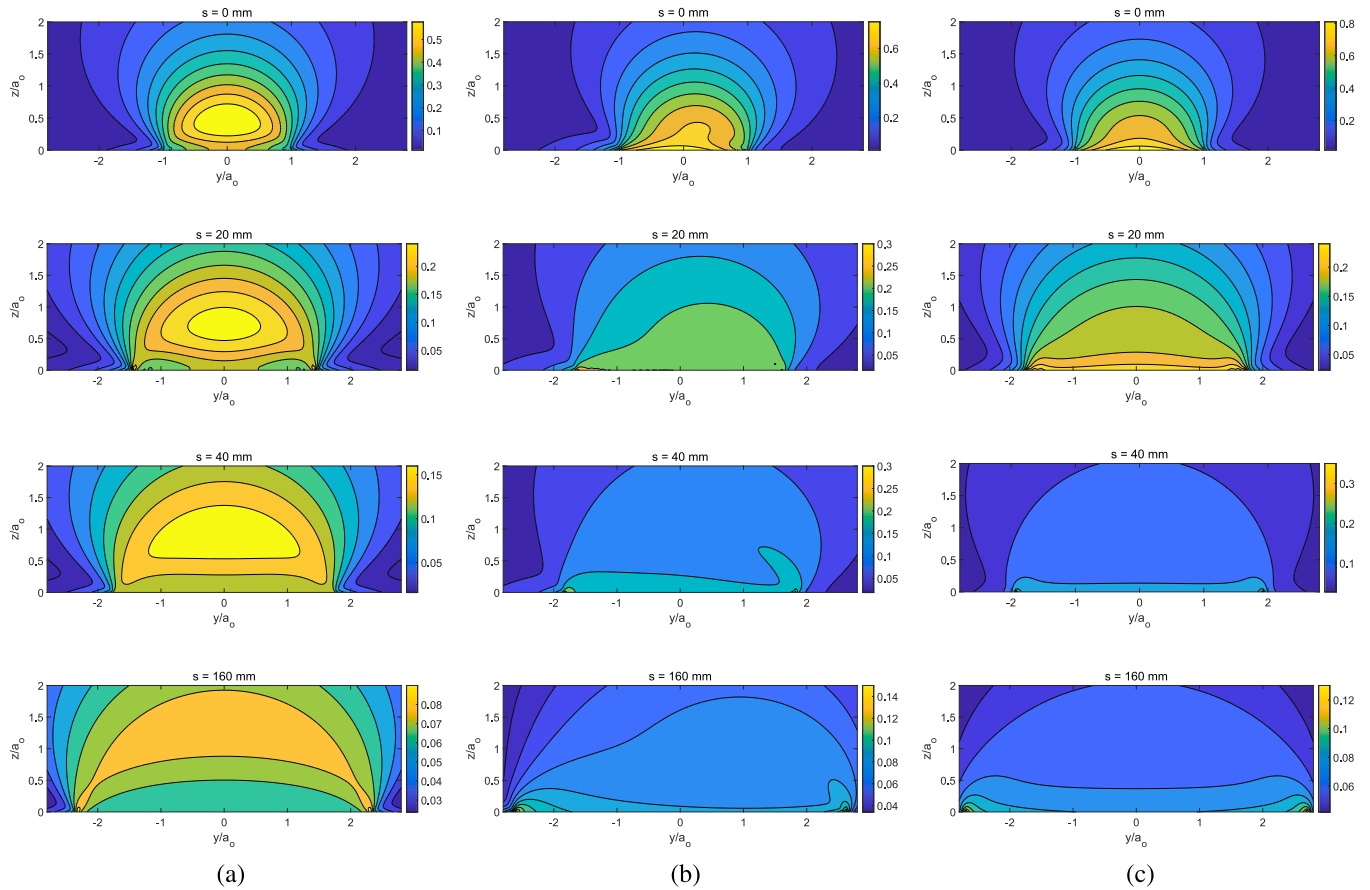
Fig. 20. Influence of the sliding direction angle on the evolution of the dimensionless Von Mises stress (σ_{VM}/p_o) distributions in the yz plane for: (a) $\beta = 0°$, (b) $\beta = 45°$ and (c) $\beta = 90°$.

$$A_{IJ}^{xx} = \frac{1}{\pi G} \left((1 - \nu) \left(k \ln \frac{m + \sqrt{k^2 + m^2}}{n + \sqrt{k^2 + n^2}} + l \ln \frac{n + \sqrt{l^2 + n^2}}{m + \sqrt{l^2 + m^2}} \right) \right.$$
$$\left. + m \ln \frac{k + \sqrt{k^2 + m^2}}{l + \sqrt{l^2 + m^2}} + k \ln \frac{l + \sqrt{l^2 + n^2}}{k + \sqrt{k^2 + n^2}} \right),$$

$$A_{IJ}^{yy} = \frac{1}{\pi G} \left((1 - \nu) \left(m \ln \frac{k + \sqrt{k^2 + m^2}}{l + \sqrt{m^2 + l^2}} + n \ln \frac{l + \sqrt{l^2 + n^2}}{k + \sqrt{n^2 + k^2}} \right) \right.$$
$$\left. + k \ln \frac{m + \sqrt{k^2 + m^2}}{n + \sqrt{k^2 + n^2}} + l \ln \frac{n + \sqrt{l^2 + n^2}}{m + \sqrt{l^2 + m^2}} \right),$$

$$A_{IJ}^{zz} = \frac{1 - \nu}{\pi G} \left(k \ln \frac{m + \sqrt{k^2 + m^2}}{n + \sqrt{k^2 + n^2}} + l \ln \frac{n + \sqrt{l^2 + n^2}}{m + \sqrt{l^2 + m^2}} \right.$$
$$\left. + m \ln \frac{k + \sqrt{k^2 + m^2}}{l + \sqrt{l^2 + m^2}} + n \ln \frac{l + \sqrt{l^2 + n^2}}{k + \sqrt{k^2 + n^2}} \right),$$

$$A_{IJ}^{xy} = \frac{\nu}{\pi G} \left(\sqrt{n^2 + k^2} - \sqrt{m^2 + k^2} + \sqrt{m^2 + l^2} - \sqrt{n^2 + l^2} \right),$$

$$A_{IJ}^{xz} = \frac{-K}{\pi G} \left(\frac{1}{2} \left(m \ln \frac{k^2 + m^2}{l^2 + m^2} + n \ln \frac{l^2 + n^2}{k^2 + n^2} \right) + k \left(\arctan \frac{m}{k} - \arctan \frac{n}{k} \right) \right.$$
$$\left. + l \left(\arctan \frac{n}{l} - \arctan \frac{m}{l} \right) \right),$$

$$A_{IJ}^{yz} = \frac{-K}{\pi G} \left(\frac{1}{2} \left(k \ln \frac{k^2 + m^2}{k^2 + n^2} + l \ln \frac{l^2 + n^2}{l^2 + m^2} \right) \right.$$
$$\left. + m \left(\arctan \frac{k}{m} - \arctan \frac{l}{m} \right) + n \left(\arctan \frac{l}{n} - \arctan \frac{k}{n} \right) \right),$$

$$A_{IJ}^{yx} = A_{IJ}^{xy}, \quad A_{IJ}^{zx} = -A_{IJ}^{xz} \text{ and } A_{IJ}^{zy} = -A_{IJ}^{yz}. \tag{41}$$

In the expressions above, $k = x_+$, $l = x_-$, $m = y_+$ and $n = y_-$, being

$$x_+ = (x_J' - x_I + \Delta_x/2), \qquad x_- = (x_J' - x_I - \Delta_x/2),$$
$$y_+ = (y_J' - y_I + \Delta_y/2), \qquad y_- = (y_J' - y_I - \Delta_y/2). \tag{42}$$

Appendix C. Explicit expression of the subsurface stresses influence coefficients

The influence coefficients to compute the subsurface stresses in $\Omega^{(\alpha)}$ ($\alpha = A, B$) have been presented in Eq. (33). They can be numerically computed according to [78] as follows.

Coefficient $(B_{ij}^N)_{IJ}$ is computed as:

$$(B_{ij}^N)_{IJ} = \frac{1}{2\pi} \left(\bar{T}_{ij}^N (x_+, y_+, z_J) + \bar{T}_{ij}^N (x_-, y_-, z_J) - \bar{T}_{ij}^N (x_-, y_+, z_J) \right.$$
$$\left. - \bar{T}_{ij}^N (x_+, y_-, z_J) \right), \tag{43}$$

being

$$\bar{T}_{xx}^N(x, y, z) = -2\nu \tan^{-1} \left(\frac{xy}{\rho z} \right) + 2(1 - 2\nu^{(\alpha)}) \tan^{-1} \left(\frac{x}{\rho + y + z} \right) - \frac{xz}{\rho(\rho + y)},$$

$$\bar{T}_{yy}^N(x, y, z) = T_{xx}^N(x, y, z),$$

$$\bar{T}_{zz}^N(x, y, z) = -\tan^{-1} \left(\frac{xy}{\rho z} \right) + \frac{xz}{\rho(\rho + y)} + \frac{yz}{\rho(\rho + x)},$$
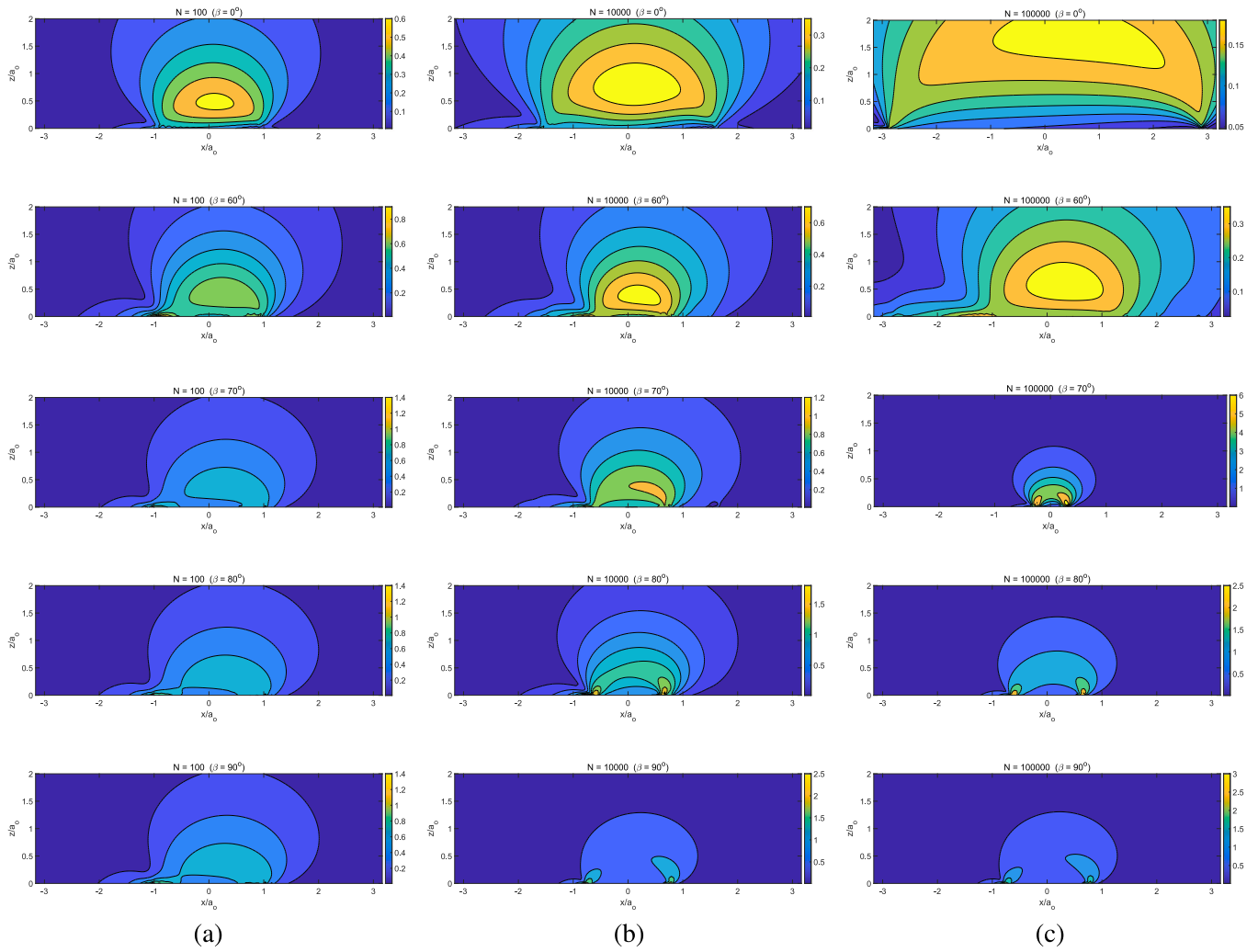
Fig. 21. Evolution of the dimensionless subsurface Von Mises stress (σ_{VM}/p_o) distributions in the xz plane after: (a) $N = 10^2$ cycles, (b) $N = 10^4$ cycles and (c) $N = 10^5$ cycles, for the following values of the sliding direction angle relative to the tribological axes, i.e., $theta = -\beta$ and $\beta = \{0°, 60°, 70°, 80°, 90°\}$.

$$\bar{T}_{xy}^{N}(x,y,z) = (2\nu - 1)ln(\rho + z) - \frac{z}{\rho},$$

$$\bar{T}_{xz}^{N}(x,y,z) = \frac{-z^2}{\rho(\rho + y)}, \tag{44}$$

$$\bar{T}_{yz}^{N}(x,y,z) = \frac{-z^2}{\rho(\rho + x)},$$

and x_+, x_-, y_+ and y_- were defined in Eq. (42). In the expressions above, it should be considered $\rho = \sqrt{x^2 + y^2 + z^2}$ and $tan^{-1}\left(\frac{xy}{\rho z}\right)|_{z=0} = \pi/2 \, sign(xy)$.

Coefficients $(B_{ij}^{Sx})_{IJ}$ are computed as:

$$
\begin{aligned}
(B_{ij}^{Sx})_{IJ} = \frac{1}{2\pi} &\left(\bar{T}_{ij}^{Sx}\left(x_+, y_+, z_J\right) + \bar{T}_{ij}^{Sx}\left(x_-, y_-, z_J\right) - \bar{T}_{ij}^{Sx}\left(x_-, y_+, z_J\right) \right. \\
&\left. - \bar{T}_{ij}^{Sx}\left(x_+, y_-, z_J\right) \right),
\end{aligned}
\tag{45}
$$

where

$$\bar{T}_{xx}^{Sx}(x,y,z) = 2ln(\rho + y) + z(1 - 2\nu^{(\alpha)})\left[\frac{y}{\rho(\rho + z)} + \frac{z}{\rho(\rho + y)}\right] - \frac{2\nu^{(\alpha)}x^2}{\rho(\rho + y)},$$

$$\bar{T}_{yy}^{Sx}(x,y,z) = 2\nu ln(\rho + y) - z(1 - 2\nu^{(\alpha)})\frac{y}{\rho(\rho + z)} - \frac{2\nu^{(\alpha)}y}{\rho},$$

$$\bar{T}_{zz}^{Sx}(x,y,z) = \frac{-z^2}{\rho(\rho + y)},$$

$$\bar{T}_{xy}^{Sx}(x,y,z) = ln(x + \rho) - z(1 - 2\nu^{(\alpha)})\frac{x}{\rho(\rho + z)} - \frac{2\nu^{(\alpha)}x}{\rho}, \tag{46}$$

$$\bar{T}_{xz}^{Sx}(x,y,z) = -\frac{xz}{\rho(\rho + y)} - tan^{-1}\left(\frac{xy}{\rho z}\right),$$

$$\bar{T}_{yz}^{Sx}(x,y,z) = \frac{-z}{\rho}.$$

Finally, coefficients $(B_{ij}^{Sy})_{IJ}$ are computed as:

$$
\begin{aligned}
(B_{ij}^{Sy})_{IJ} = \frac{1}{2\pi} &\left(\bar{T}_{ij}^{Sy}\left(x_+, y_+, z_J\right) + \bar{T}_{ij}^{Sy}\left(x_-, y_-, z_J\right) - \bar{T}_{ij}^{Sy}\left(x_-, y_+, z_J\right) \right. \\
&\left. - \bar{T}_{ij}^{Sy}\left(x_+, y_-, z_J\right) \right),
\end{aligned}
\tag{47}
$$

being

$$\bar{T}_{xx}^{Sy}(x,y,z) = \bar{T}_{yy}^{Sx}(y,x,z),$$

$$\bar{T}_{yy}^{Sy}(x,y,z) = \bar{T}_{xx}^{Sx}(y,x,z),$$

$$\bar{T}_{zz}^{Sy}(x, y, z) = \bar{T}_{zz}^{Sx}(y, x, z),$$
$$\bar{T}_{xy}^{Sy}(x, y, z) = \bar{T}_{xy}^{Sx}(y, x, z),$$
$$\bar{T}_{xz}^{Sy}(x, y, z) = \bar{T}_{yz}^{Sx}(y, x, z),$$
$$\bar{T}_{yz}^{Sy}(x, y, z) = \bar{T}_{xz}^{Sx}(y, x, z).$$

(48)

Appendix D. Subsurface stress distribution and evolution under isotropic sliding wear conditions

Fig. 19 presents the evolution of the dimensionless Von Mises stress (σ_{VM}/p_o) distributions in the xz plane as a function of the sliding wear distance, assuming isotropic friction and wear conditions. The stresses distributions in Fig. 19 are presented for $\mu = \{0, 0.25, 0.50\}$, and the nondimensional sliding distances: $s/a_o = \{0, 20/3, 800/3, 3200/3\}$. The x and z coordinates are expressed relative to the initial contact semi-width ($a_o = 0.15$ mm).

Appendix E. Subsurface stress distribution and evolution under orthotropic sliding wear conditions

Fig. 20 presents the evolution of the dimensionless Von Mises stress (σ_{VM}/p_o) distribution in the yz plane for the following values of the sliding direction angle relative to the tribological axes, i.e., $\theta = -\beta$ ($\beta = \{0°, 45°, 90°\}$), and the nondimensional sliding distances: $s/a_o = 0$, $s/a_o = 20/3$, $s/a_o = 800/3$ and $s/a_o = 3200/3$. The x and z coordinates are expressed relative to the initial contact semi-width ($a_o = 0.15$ mm).

Appendix F. Subsurface stress distribution and evolution under orthotropic fretting wear conditions

Fig. 21 presents the dimensionless subsurface Von Mises stress (σ_{VM}/p_o) distributions in the xz plane after $N = \{10^2, 10^4, 10^5\}$ cycles, considering the following values of the sliding direction angle relative to the tribological axes, i.e., $\theta = -\beta$ and $\beta = \{0°, 60°, 70°, 80°, 90°\}$.

References

[1] Rabinowicz E. Friction and wear of materials. John Wiley & Sons; 1965.

[2] Hertz H. On the contact of elastic solids. MacMillan, London: Miscellaneous Papers; 1881/1896.

[3] Cattaneo C. Sul contatto di due corpi elastici: distribuzione locale degli sforzi. Rend Accad Naz Lincei 1938;27:342–8.

[4] Mindlin RD. Compliance of elastic bodies in contact. J Appl Mech 1949;16:259–68.

[5] Johnson KL. Contact mechanics. Cambridge: Cambridge University Press; 1987.

[6] Goryacheva IG. Contact mechanics in tribology. Springer; 1998.

[7] Kikuchi N, Oden JT. Contact problems in elasticity: A study of variational inequalities and finite element methods. SIAM, Philadelphia, USA: SIAM; 1987.

[8] Kalker JJ. Three-dimensional elastic bodies in rolling contact. The Netherlands: Kluwer Academic Publisher; 1990.

[9] Wriggers P. Computational contact mechanics. Spriger; 2006.

[10] Laursen TA. Computational contact and impact mechanics. England: Springer; 2002.

[11] Hueber S, Stadler G, Wohlmuth BI. A primal–dual active set algorithm for three-dimensional contact problems with Coulomb friction. SIAM J Sci Comput 2008;30:572–96.

[12] Man KW. Contact mechanics using boundary elements. Boston, MA: Computational Mechanics Publisher; 1994.

[13] Kalker JJ, Jacobson B. Rolling contact phenomena. Springer Vienna; 2000.

[14] Willner K. Fully coupled frictional contact using elastic halfspace theory. J Tribol 2008;130(3).

[15] Pohrt R, Li Q. Complete boundary element formulation for normal and tangential contact problems. Phys Mesomech 2014;17:334–40.

[16] Liu S, Wang Q. Studying contact stress fields caused by surface tractions with a discrete convolution and fast Fourier transform algorithm. J Tribol 2002;124:36–45.

[17] Wang QJ, Zhu D. Hertz theory: Contact of ellipsoidal surfaces. Encycl Tribol 2013;1647–54.

[18] Jin X, Niu F, Zhang X, Zhou Q, Lyu D, Keer LM, et al. Love's rectangular contact problem revisited: A complete solution. Tribol Int 2016;103:331–42.

[19] Holm R. Electric contacts. Stockholm: Almquist and Wiksells Akademiska Handböcker; 1946.

[20] Archard JF. Contact and rubbing of flat surfaces. J Appl Phys 1953;24:981–8.

[21] Galin LA. Contact problems of the theory of elasticity in the presence of wear. J Appl Math Mech 1976;40(6):931–6.

[22] Galin LA, Goryacheva IG. Axisymmetric contact problem of the theory of elasticity oin the presence of wear. J Appl Math Mech 1977;41:826–31.

[23] Aleksandrov VM, Kovalenko EV. Plane conact problems of the theory of elasticity for nonclassical regions in the presence of wear. J Appl Mech Tech Phys 1980;3:421–427.

[24] Kovalenko EV. Study of the axisymmetric contact problem of the wear of a pair consisting of an annular stamp and a rough half-space. J Appl Math Mech 1985;49:641–7.

[25] Kragelsky IV. Friction and wear calculation methods. Oxford, UK: Pergamon Press; 1982.

[26] Komogortsev VF. Contact between a moving stamp and an elastic half-plane when there is wear. J Appl Math Mech 1985;49:243–6.

[27] Hills DA, Fellows LJ. Some observations on contact problems involving fretting in the presence of wear. Wear 1999;231(2):319–24.

[28] Hills DA, Sackfield A, Paynter RJH. Simulation of fretting wear in half-plane geometries. Part 1. The solution for long term wear. J Tribol 2009;131:031401, (4 pages).

[29] Goryacheva IG, Rajeev PT, Farris TN. Wear in partial slip contact. J Tribol 2001;123:848–56.

[30] Olofsson U, Andersson S, Bjorklund S. Simulation of mild wear in boundary lubricated spherical roller thrust bearing. Wear 2000;241:180–5.

[31] Enblom R, Berg M. Simulation of railway wheel profile development due to wear-influence of disc braking and contact environment. Wear 2005;258:1055–63.

[32] Telliskivi T. Simulation of wear in a rolling-sliding contact by a semi-Winkler model and the Archard's wear law. Wear 2004;256:817–31.

[33] Hegadekatte V, Kurzenhäuser S, Kraft OA. Predictive modeling scheme for wear in tribometers. Tribol Int 2008;41:1020–31.

[34] Argatov II. Asymptotic modeling of reciprocating sliding wear with application to local interwire contact. Wear 2011;271:1147–55.

[35] Argatov II, Tato W. Asymptotic modeling of reciprocating sliding wear - comparison with finite-element simulations. Eur J Mech A Solids 2012;34:1–11.

[36] Argatov II, Chai YS. Effective wear coefficient and wearing-in period for a functionally graded wear-resisting punch. Acta Mech 2019;230:2295–307.

[37] Argatov II, Chai YS. Wear contact problem with friction: Steady-state regime and wearing-in period. Int J Solids Struct 2020;193–194:213–21.

[38] Argatov II, Tato W. Contact geometry adaptation in fretting wear: A constructive review. Front Mech Eng 2020;6:51.

[39] Yue T, Wahab MA. A review on fretting wear mechanisms models and numerical analyses. Comput Mater Contin 2019;59:405–32.

[40] Johansson L. Numerical simulation of contact pressure evolution in fretting. J Tribol 1994;116:247–54.

[41] Strömberg N, Johansson L, Klarbring A. Derivation and analysis of a generalized standard model for contact, friction and wear. Int J Solids 1996;33(13):1817–36.

[42] Strömberg N. An augmented lagrangian method for fretting problems. Eur J Mech A Solids 1997;16(4):573–93.

[43] Strömberg N. Newton method for three-dimensional fretting problems. Int J Solids Struct 1999;36(4):2075–90.

[44] Ireman P, Klarbring A, Strömberg N. A model of damage coupled to wear. J Solids Struct 2003;40:2957–74.

[45] Ireman P, Klarbring A, Stromberg N. Finite element algorithms for thermoelastic wear problems. J Mech A Solids 2002;21:423–40.

[46] Ireman P, Klarbring A, Strömberg N. Gradient theory of damage coupled to frictional contact and wear, and its numerical treatment. CMES 2009;52:125–58.

[47] McColl IR, Ding J, Leen SB. Finite element simulation and experimental validation of fretting wear. Wear 2004;256:1114–27.

[48] Chai YS, Lee CY, Bae JW, Lee SY, Hwang JK. Finite element analysis of fretting wear problems in consideration of frictional contact. Key Eng Mater 2005;297–300:1406–11.

[49] Mary C, Fouvry S. Numerical prediction of fretting contact durability using energy wear approach: optimisation of finite-element model. Wear 2007;263:444–50.

[50] Bae JW, Lee CY, Chai YS. Three dimensional fretting wear analysis by finite element substructure method. Int J Precis Eng Manufact 2009;10:63–9.

[51] Paczelt I, Mróz Z. Optimal shapes of contact interfaces due to sliding wear in the steady relative motion. Int J Solids Struct 2007;44:895–925.

[52] Farah P, Wall WA, Popp A. An implicit finite wear contact formulation based on dual mortar methods. Internat J Numer Methods Engrg 2017;111:325–53.

[53] Doca T, Andrade Pires FM. Finite element modeling of wear using the dissipated energy method coupled with a dual mortar contact formulation. Comput Struct 2017;191:62–79.

[54] Sfantos GK, Aliabadi MH. Application of BEM and optimization technique to wear problems. Int J Solids Struct 2006;43:3626–42.

[55] Sfantos GK, Aliabadi MH. Wear simulation using an incremental sliding boundary element method. Wear 2006;260:1119–28.

[56] Sfantos GK, Aliabadi MH. A boundary element formulation for three dimensional sliding wear simulation. Wear 2007;262:672–83.

[57] Paczelt I, Kucharski S, Mróz Z. The experimental and numerical analysis of quasi-steady wear processes for a sliding spherical indenter. Wear 2012;274–275:127–48.

[58] Nowell D. Simulation of fretting wear in half-plane geometries. Part II. Analysis of the transient wear problem using quadratic programming. J Tribol 2010;132:021402, (8 pages).

[59] Gallego L, Nelias D, Deyber S. A fast and efficient contact algorithm for fretting problems applied to fretting modes i, ii and iii. Wear 2010;268(1-2):208–22.

[60] Kim TW, Moon SM, Cho YJ. Prediction of fretting wear using boundary element method. Tribol Int 2011;44:1571–6.

[61] Rodríguez-Tembleque L, Abascal R, Aliabadi MH. A boundary element formulation for 3D fretting-wear problems. Eng Anal Bound Elem 2011;35:935–43.

[62] Rodríguez-Tembleque L, Aliabadi MH. Numerical simulation of fretting wear in fiber-reinforced composite materials. Eng Fract Mech 2016;168:13–27.

[63] Rodríguez-Tembleque L, Abascal R, Aliabadi MH. A boundary element formulation for wear modeling on 3D contact and rolling-contact problems. Int J Solids Struct 2010;47:2600–12.

[64] Rodríguez-Tembleque L, Abascal R, Aliabadi MH. Anisotropic wear framework for 3D contact and rolling problems. Comput Methods Appl Mech Engrg 2012;241:1–19.

[65] Güler MA, Kucuksucu A, Yilmaz KB, Yildrim B. On the analytical and finite element solution of plane contact problem of a rigid cylindrical punch sliding over a functionally graded orthotropic medium. Int J Mech Sci 2016;120:12–29.

[66] Meshcheryakova AR, Goryacheva IG. Stress state of elastic bodies with an intermediate layer in rolling contact with slip. Phys Mesomech 2021;23:91–101.

[67] Fereidouni H, Akbarzadeh S, Khonsari MM. The relation between subsurface stresses and useful wear life in sliding contacts. Tribol Lett 2020;68(9).

[68] Rodríguez-Tembleque L, Abascal R. Fast FE-BEM algorithms for orthotropic frictional contact. Int J Numer Methods Engng 2013;94:687–707.

[69] Michalowski R, Mróz Z. Associated and non-associated sliding rules in contact friction problems. Archiwum Mechaniki Stosowanej 1978;30:259–76.

[70] Mróz Z, Stupkiewicz S. An anisotropic friction and wear model. Int J Solids Struct 1994;31:1113–31.

[71] Mróz Z, Kucharski S, Paczelt I. Anisotropic friction and wear rules with account for contact state evolution. Wear 2018;396:1–11.

[72] McColl IR, J Ding, Leen SB. Finite element simulation and experimental validation of fretting wear. Wear 2004;256:1114–27.

[73] Paczelt I, Kucharski S, Mróz Z. The experimental and numerical analysis of quasi-steady wear processes for a sliding spherical indenter. Wear 2012;274–275:127–48.

[74] Paczelt I, Mróz Z. Solution of wear problems for monotonic and periodic sliding with p-version of the finite element method. Comput Meth Appl Mech Engng 2012;249–252:75–103.

[75] Stupkiewicz S. An ALE formulation for implicit time integration of quasi-steady-state wear problems. Comput Meth Appl Mech Engng 2013;260:130–42.

[76] Cavalieri JF, Cardona A. Three-dimensional numerical solution for wear prediction using a mortar contact algorithm. Int J Numer Methods Engng 2013;96:467–86.

[77] Lengiewicz J, Stupkiewicz S. Efficient model of evolution of wear in quasi-steady-state sliding contacts. Wear 2013;303:611–21.

[78] Wang QY, Bathias C, Kawagoishi N, Chen Q. Effect of inclusion on subsurface crack initiation and gigacycle fatigue strength. Int J Fatigue 2002;24:1269–74.

[79] Rodríguez-Tembleque L, Buroni FC, Sáez A. 3D BEM for orthotropic frictional contact of piezoelectric bodies. Comput Mech 2015;56:491–502.

[80] Rodríguez-Tembleque L, Buroni FC, Sáez A, Aliabadi MH. 3D coupled multifield magneto-electro-elastic contact modelling. Int J Mech Sci 2016;114:35–51.

[81] Joli P, Feng Z-Q. Uzawa and newton algorithms to solve frictional contact problems within the bi-potential framework. Internat J Numer Methods Engrg 2008;73:317–30.

[82] Ning P, Feng Z-Q, Quintero JAR, Zhou Y-J, Peng L. Uzawa algorithm to solve elastic and elastic–plastic fretting wear problems within the bipotential framework. Comput Mech 2018;62(6):1327–41.